Monthly Notices of the ROYAL ASTRONOMICAL SOCIETY

MNRAS **548,** 1–26 (2026) https://doi.org/10.1093/mnras/stag616
Advance Access publication 2026 March 28

MIGHTEE: the evolving radio luminosity functions of star-forming galaxies to $z \sim 4.5$ and the cosmic history of star formation

Nijin J. Thykkathu [1,2★] Matt J. Jarvis [1,3] Imogen H. Whittam [1,3] C. L. Hale,[1,4] A. M. Matthews,[5] I. Heywood,[1,6,7,8] Eliab Malefahlo [9], R. G. Varadaraj [1] N. Stylianou [1] Chris Pearson [1,2,10] Nick Seymour [11] and Mattia Vaccari [12,13,14]

[1]*Astrophysics, Department of Physics, University of Oxford, Keble Road, Oxford OX1 3RH, UK*
[2]*RAL Space, UKRI STFC Rutherford Appleton Laboratory, Chilton, Didcot, Oxfordshire OX11 0QX, UK*
[3]*Department of Physics and Astronomy, University of the Western Cape, Robert Sobukwe Road, 7535 Bellville, Cape Town, South Africa*
[4]*Institute for Astronomy, University of Edinburgh, Royal Observatory, Blackford Hill, Edinburgh EH9 3HJ, UK*
[5]*Carnegie Observatories, 813 Santa Barbara Street, Pasadena, CA 91101, USA*
[6]*Department of Physics and Electronics, Rhodes University, PO Box 94, Makhanda 6140, South Africa*
[7]*SKA Observatory, Jodrell Bank, Lower Withington, Macclesfield SK11 9FT, UK*
[8]*South African Radio Astronomy Observatory, Liesbeek House, River Park, Gloucester Road, Mowbray 7700, South Africa*
[9]*UNISA Centre for Astrophysics and Space Sciences, College of Science, Engineering and Technology, University of South Africa, Cnr Christian de Wet Rd and Pioneer Avenue, Florida Park, 1709 Roodepoort, South Africa*
[10]*Department of Physical Sciences, The Open University, Milton Keynes MK7 6AA, UK*
[11]*International Centre for Radio Astronomy Research, Curtin University, GPO Box U1987, Bentley WA 6845, Australia*
[12]*Inter-University Institute for Data Intensive Astronomy, Department of Astronomy, University of Cape Town, 7701 Rondebosch, Cape Town, South Africa*
[13]*Department of Physics and Astronomy, University of the Western Cape, 7535 Bellville, Cape Town, South Africa*
[14]*INAF – Istituto di Radioastronomia, via Gobetti 101, I-40129 Bologna, Italy*

Accepted 2026 March 26. Received 2026 March 11; in original form 2026 January 20

ABSTRACT

A key question in extragalactic astronomy is how the star formation rate density (SFRD) evolves over cosmic time. A powerful way of addressing this question is using radio-continuum observations, where the radio waves are unaffected by dust and are able to reach sufficient resolution to resolve individual galaxies. We present an investigation of the 1.4 GHz radio luminosity functions (RLFs) of star-forming galaxies (SFGs) and active galactic nuclei (AGNs) using deep radio continuum observations in the COSMOS and XMM–LSS fields, covering a combined area of $\sim 4\,\mathrm{deg}^2$. These data enable the most accurate measurement of the evolution in the SFRD from mid-frequency radio continuum observations. We model the total RLF as the sum of evolving SFG and AGN components, negating the need for individual source classification. We find that the SFGs have systematically higher space densities at fixed luminosity than found in previous radio studies, but consistent with more recent studies with MeerKAT. We attribute this to the excellent low-surface brightness sensitivity of MeerKAT. We then determine the evolution of the SFRD. Adopting the far-infrared–radio correlation results in a significantly higher SFRD at $z > 1$, compared to combined UV and far-infrared measurements. However, using more recent relations for the correlation between star formation rate and radio luminosity, based on full spectral energy distribution modelling, can resolve this apparent discrepancy. Thus, radio observations provide a powerful method of determining the total SFRD in the absence of dust-sensitive far-infrared data.

Key words: galaxies: active – galaxies: evolution – galaxies: star formation – radio continuum: galaxies.

1 INTRODUCTION

The cosmological evolution of star-forming galaxies (SFGs) and active galactic nuclei (AGNs) is critically important for our general understanding of the evolution of galaxies and the build-up of structure in the Universe. Galaxy evolution is a combination of long-term interactions between internal and external environmental processes, involving the stars, gas clouds, morphological structure, and the small and large-scale environment. All of these can influence the level of star formation (SF) and AGN activity.

In the last decade, multiwavelength observations of galaxy populations have increased dramatically, but there is still no clear understanding of the core mechanisms that control the star formation rate (SFR) histories of individual galaxies. One of the reasons is that it is not possible to follow individual galaxies throughout their evolution, and statistical methods that investigate many galaxies at different epochs have to be used. These studies are fur-

★ E-mail: nijin.thykkathu@physics.ox.ac.uk

ther complicated by the vast array of selection biases depending on the wavelength that is used for the observations, coupled with how measurements at these wavelengths translate to estimates of physical properties, such as SFR (e.g. R. C. Kennicutt 1998; R. C. Kennicutt & N. J. Evans 2012).

The radio continuum emission observed in SFGs primarily arises from synchrotron radiation, a phenomenon originating from the acceleration of high-energy electrons within supernova remnants. These electrons gain energy through interactions within the remnants, particularly during the cataclysmic explosions that occur when massive stars undergo supernova events. This synchrotron emission mechanism tends to dominate the radio emission spectrum at rest-frame frequencies of < 30 GHz (J. J. Condon 1992a). The radio emission emanating from SFGs exhibits a strong correlation with the far-infrared (FIR) emission, a relationship commonly referred to as the FIR–radio correlation (M. S. Yun, N. A. Reddy & J. J. Condon 2001; M. J. Jarvis et al. 2010; S. C. Read et al. 2018; H. S. B. Algera et al. 2020) and, given the FIR emission is a good tracer of the SFR in galaxies, the SFR–radio correlation (e.g. E. F. Bell 2003; L. Wang et al. 2019; D. J. B. Smith et al. 2021a, b; R. H. W. Cook et al. 2024).

Furthermore, such measurements are not affected by dust obscuration, thus potentially leading to an unbiased view of the star formation history of the Universe, providing semi-independent measurements of the cosmic star formation rate density (SFRD) up to $z \sim 2$ that can also be traced by combining UV, optical and FIR wavelengths (e.g. A. Karim et al. 2011; M. Novak et al. 2017; E. D. Malefahlo et al. 2022; F. Gentile et al. 2025). Recently, using extremely deep radio continuum observations, R. K. Cochrane et al. (2023) and A. M. Matthews et al. (2024) have shown that the SFRD traced by radio emission may actually exceed that from UV and FIR tracers at $z < 1.5$.

As we move to higher redshifts ($z > 3$), inverse Compton scattering of the Cosmic Microwave Background photons may also become important (e.g. E. J. Murphy 2009). Indeed, evidence for this has recently been found from stacking the radio emission from high-redshift Lyman-break galaxies, leading to a relative decrease in the observed radio continuum emission at a given SFR (I. H. Whittam et al. 2025). As such, determining the evolving SFRD at even earlier epochs may present different challenges.

As efforts are made to utilize radio emission as a reliable indicator of SF activity, a significant challenge arises when attempting to discern the contribution of AGN to the observed radio emission. This radio emission can often be mis-associated with the emission originating from SF processes (and vice versa) (e.g. A. E. Kimball et al. 2011; J. J. Condon et al. 2013; S. V. White et al. 2015, 2017; E. Malefahlo et al. 2020; C. Macfarlane et al. 2021; B. H. Yue et al. 2025), all of which highlight the problem of measuring the star formation contribution in optically selected radio-quiet quasars, which are known to have an AGN, are not selected via their radio emission, but still often have detectable radio emission. The situation can become even more complicated for radio-selected samples, where it is not known a priori whether the radio sources have an AGN at all. This potential confusion necessitates careful consideration and analysis to disentangle the distinct sources of radio emission and to accurately interpret the underlying astrophysical phenomena. The most robust method to account for this is with sensitive high-resolution studies and with very long baseline interferometry (e.g. T. W. B. Muxlow et al. 2020; J. F. Radcliffe et al. 2021; L. K. Morabito et al. 2025). However, such data are often limited to small areas and have relatively poor surface brightness sensitivity.

It has been known for several decades that high radio luminosity AGN ($L_{\rm rad} \gtrsim 10^{25}\,{\rm W\,Hz^{-1}}$) evolve positively, meaning they become more common at higher redshift (e.g. J. S. Dunlop & J. A. Peacock 1990; M. J. Jarvis et al. 2001; C. J. Willott et al. 2001; E. E. Rigby et al. 2011), in a similar way to the cosmic SFRD. These AGN can also have a significant impact on galaxy evolution, where AGN outflows are often posited as being responsible for controlling or terminating SF (e.g. A. Cattaneo et al. 2009; P. N. Best & T. M. Heckman 2012; A. C. Fabian 2012; T. M. Heckman & P. N. Best 2014; M. J. Hardcastle & J. H. Croston 2020; R. Kondapally et al. 2023; T. M. Heckman et al. 2024). On the other hand, the evolution of low-luminosity ($L_{\rm rad} \lesssim 10^{25}$) AGN is not as well understood and some studies suggest that there is no evolution of the radio luminosity function (L. Clewley & M. J. Jarvis 2004), whereas some suggested they do evolve but slowly compared to the high-luminosity AGN (V. Smolčić et al. 2009; K. McAlpine & M. J. Jarvis 2011; R. Kondapally et al. 2022).

We note that a simple division into high- and low-luminosity radio AGN does not uniquely correspond to physically distinct accretion modes. A more physically motivated distinction is between High-Excitation Radio Galaxies (HERGs) and Low-Excitation Radio Galaxies (LERGs; T. M. Heckman & P. N. Best 2014). These populations differ in their accretion properties and optical spectra, but they overlap substantially in radio luminosity (e.g. M. B. Pracy et al. 2016). Since HERGs are known to evolve more strongly with redshift than LERGs, the overall shape of the AGN RLF may change with cosmic time relative to its local form; however, the spectroscopic data are often not available or complete enough to disentangle such effects over large redshift baselines.

At low-redshift ($z \lesssim 0.2$), volume-limited samples of radio sources with complete redshift information and classification of sources into star-forming or AGN-dominated can be achieved using optical emission lines. T. Mauch & E. M. Sadler (2007) used 7824 radio sources divided into SFGs and AGNs using optical spectroscopy, revealing that SFGs dominate the local radio luminosity function below $L_{1.4\rm GHz} < 10^{23}\,{\rm WHz^{-1}}$, whereas AGN dominate above this threshold. However, at higher redshifts, complete spectroscopy becomes more difficult to obtain and the emission lines used for distinguishing SFGs and AGN can be redshifted beyond the optical window, particularly at $z > 1$. However, recent work using the overlap of the Dark Energy Spectroscopic Instrument (DESI; DESI Collaboration 2024) and the LOFAR two-metre sky survey deep fields (J. Sabater et al. 2021; C. Tasse et al. 2021) shows that this is now possible to $z \sim 1$ (e.g. M. I. Arnaudova et al. 2025).

One method of avoiding the pitfalls in classifying radio sources into AGN and/or SFGs, in order to measure their evolution, is by measuring the complete radio luminosity function with a flexible enough parametrization that allows for the contributions from both populations to be represented. This has been done at both radio wavelength (e.g K. McAlpine, M. J. Jarvis & D. G. Bonfield 2013) and for the rest-frame UV luminosity function (e.g. N. J. Adams et al. 2023).

Modelling the total RLF provides a statistical framework for separating SFGs and AGN based on their radio emission. By constructing separate RLF models for SFGs and AGN, but by fitting for them jointly, we can characterize the luminosity distribution for each population across different redshifts. Importantly, this

method does not rely on classifications for every sources, but aims to understand the evolution of the populations as a whole, through statistical separation. In this paper, we adopt this strategy to measure the evolving radio-luminosity function using data from the MeerKAT International GHz Tiered International Exploration (MIGHTEE; M. Jarvis et al. 2016) survey.

This paper is organised as follows. In Section 2, we describe the MeerKAT data and the multiwavelength ancillary data used throughout this work. Section 3 outlines the completeness corrections applied. In Section 4, we describe the methods to measure and model RLFs and their evolution over cosmic time. In Section 5, we present the results of our fits to the RLFs of both SFGs and AGN and discuss how this translates to measurements of the evolution in the cosmic SFRD. Finally, in Section 6, we summarize our results and present our conclusions.

Throughout this paper, we adopt the following cosmological parameters: $H_0 = 70\ \mathrm{km\,s^{-1}\,Mpc^{-1}}$, $\Omega_\mathrm{M} = 0.3$, and $\Omega = 0.7$. All magnitudes are AB magnitudes unless stated otherwise (J. B. Oke & J. E. Gunn 1983). We assume a spectral index defined as $S_\nu \propto \nu^\alpha$, with $\alpha = -0.7$, when converting flux density (S_ν) to luminosity at a rest-frame frequency of 1.4 GHz. Logarithms are base 10 unless stated otherwise.

2 DATA AND SAMPLE SELECTION

In this paper, we use the Early Science data in the COSMOS and the XMM–LSS fields from the MIGHTEE survey. For more details about the data and the observations, please refer to I. Heywood et al. (2022). The COSMOS observations consist of a single pointing with the MeerKAT telescope, covering $\sim$1.6 deg^2 down to a limiting thermal noise of $\sim$2 μJy beam^{-1} at L-band. The larger XMM–LSS field consists of three overlapping pointings, covering $\sim$3.5 deg^2. Two versions of the Stokes I image (and associated data products) are produced, one with higher sensitivity and slightly poorer resolution and one for higher resolution at the expense of sensitivity. The maximum sensitivity image was produced with Briggs robust = 0.0, has synthesized beam size = 8.6 × 8.6 arcsec^2 and thermal noise $\sim$2 μJy beam^{-1}. Although due to classical confusion, these observations are limited to a total noise of approximately 4μJy beam^{-1} at the centre of the primary beam. The higher resolution image was produced with Briggs robust = −1.2, has a synthesized beam size $\sim$5 × 5 arcsec^2 and thermal noise $\sim$6 μJy beam^{-1}. Due to the wide bandwidth of the MeerKAT $L-$band receiver, the effective frequency varies across the primary beam and I. Heywood et al. (2022) provide an effective frequency map for each image, which gives the effective frequency at each pixel. Source extraction was conducted using the Python Blob Detection and Source Finder (PyBDSF; N. Mohan & D. Rafferty 2015) with the default parameters in I. Heywood et al. (2022). The extracted catalogue contains 30 170 radio components across the two fields: 9896 in COSMOS and 20 274 in XMM–LSS.

We use the cross-matched catalogues provided by I. H. Whittam et al. (2024) for the COSMOS field and S. Zhu et al. (2023) for the XMM–LSS field, to associate the sources with an optical counterpart. We associate these sources with the photometric redshifts determined using the Le Phare (O. Ilbert et al. 2009) spectral energy distribution fitting code combined with machine-learning photometric redshifts using GPz (I. A. Almosallam et al. 2016a; I. A. Almosallam, M. J. Jarvis & S. J. Roberts 2016b) as detailed in P. W. Hatfield et al. (2022), following similar work (K. J. Duncan et al. 2018, 2021).

Specifically, we use optical data from the Canada–France–Hawaii-Telescope Legacy Survey (CFHTLS; J.-C. J. Cuillandre et al. 2012), and the HyperSuprimeCam Strategic Survey Programme (HSC DR2; H. Aihara et al. 2018a, b, 2019). The corresponding near-infrared data in the XMM-LSS field are from the VISTA Deep Extragalactic Observations (VIDEO) survey (M. J. Jarvis et al. 2013), while UltraVISTA DR6 (H. J. McCracken et al. 2012) provides the near-infrared coverage in COSMOS. For further details, we refer the reader to R. A. A. Bowler et al. (2021), N. J. Adams et al. (2023), and R. G. Varadaraj et al. (2023, 2026). We use the full probability distribution function (PDF) for the photometric redshifts to measure the RLF accounting for uncertainties in redshift.

Spectroscopic redshifts are available over both fields from a range of surveys and we use the updated compilation from A. A. Khostovan et al. (2026) in COSMOS and also from M. Vaccari (2022), which include more recent data. We also include additional spectroscopic redshifts from the DESI (DESI Collaboration 2024). For radio sources where spectroscopic redshifts are available, we use these, otherwise photometric redshifts are adopted.

We are unable to obtain reliable redshifts in regions where the optical/near-infrared imaging is compromised by bright stars and associated artefacts. We therefore apply a bright–star and coverage mask to the radio footprints in the MIGHTEE Early-Science COSMOS and XMM–LSS fields, excluding radio sources that fall inside masked pixels. The resulting effective area for each field is $\simeq 0.83$ deg^2 (COSMOS) and $\simeq 3.23$ deg^2 (XMM–LSS), giving a combined area of $\simeq 4.06$ deg^2.

We adopt a conservative flux-density cut at 40μJy (around 8–10σ across both fields) to mitigate against confusion and significant completeness corrections (see Section 3). With this flux-density limit and after masking, 6039 radio sources remain in COSMOS. Of these, 830 lack an optical/NIR counterpart from the visually inspected catalogue of I. H. Whittam et al. (2024), yielding $C_\mathrm{opt} = 86.3$ per cent. In the XMM–LSS field, 17,666 of 18,796 sources at $S > 40\mu$Jy have an optical/NIR counterpart from the catalogue of S. Zhu et al. (2023). We note that the higher completeness in the XMM–LSS field arises from the different approaches to the cross-matching, with the approach taken in I. H. Whittam et al. (2024) being more conservative than that used by S. Zhu et al. (2023). However, we note that we correct for the incompleteness due to missing counterparts in both fields in a similar way (see Section 3.2), and the difference between the source cross-matching has a negligible effect on our results. The redshift distributions for both the COSMOS and XMM-LSS fields, denoting the spectroscopic versus photometric redshifts, are shown in Fig. 1

Deep radio surveys may contain a small fraction of very extended sources, where in some cases the lobes of large-angular sized AGN may be mis-identified as distinct sources. Identifying the correct optical host for such systems requires associating the individual radio components, often by eye, as done for the sample used here (I. H. Whittam et al. 2024). It is still possible that some radio sources without optical counterparts are components of larger systems whose true optical counterparts lie at large angular separations, possibly associated with a core. However, we expect this to be a negligible fraction of the radio sources without optical counterparts, due to both the relative rarity of extended AGN and the excellent surface brightness sensitivity of MeerKAT, which can often detect the faint diffuse emission that connects a core to a lobe (e.g. J. Delhaize et al. 2021).

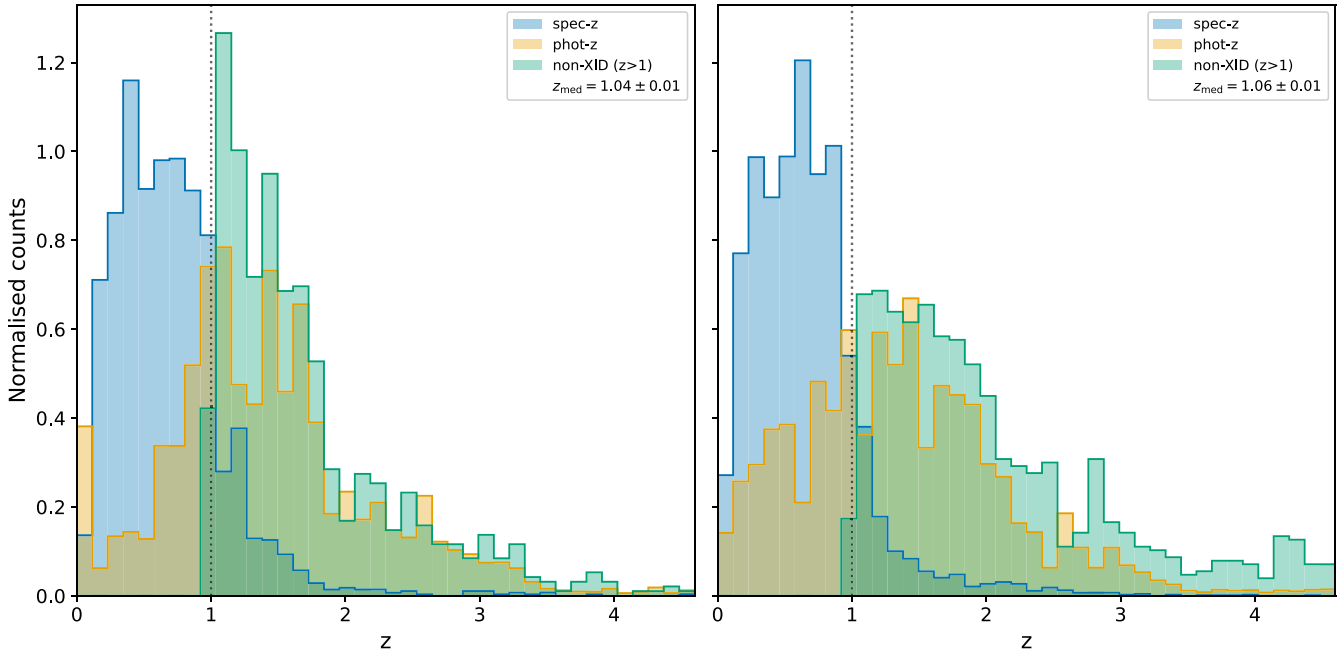

Figure 1. Normalised Redshift distributions for radio sources in the COSMOS (left) and XMM–LSS (right) fields. Each panel shows the normalised redshift histograms for sources with spectroscopic redshifts (spec-z; blue), photometric redshifts where no spec-z is available (phot-z; orange), and radio sources without optical counterparts plotted at z>1 (nonXID; green). Non-XID sources are assigned redshifts using the flux-dependent method described in Section 3.2 and are shown here restricted to z>1. The median redshifts are $z_{\rm med} = 1.04 \pm 0.01$ (COSMOS) and $z_{\rm med} = 1.06 \pm 0.01$ (XMM–LSS).

By combining both the COSMOS and XMM–LSS field, we reduce the level of cosmic variance due to the large-scale structure of the Universe. However, at the lowest redshifts in our study, this may still be significant. We therefore use the cosmic variance calculator in B. P. Moster et al. (2011) to estimate the expected cosmic variance in the two fields and in the combined fields. The cosmic variance increases with the galaxy bias, and we expect the low-mass galaxies that dominate the faint end of the SFG population to have relatively low bias, whereas the more massive galaxies that host the radio-AGN in our sample are likely to be the most highly biased (see e.g. S. N. Lindsay et al. 2014; M. Magliocchetti et al. 2017; C. L. Hale et al. 2018; G. C. Petter et al. 2024; J. Hamlett et al. 2026).

In our lowest redshift bin of $0.2 < z < 0.4$, with the lowest co-moving volume, the cosmic variance in the expected number density of these populations spans 12–18 per cent in the COSMOS field and 8–14 per cent in the larger XMM–LSS field. For the combined area, the cosmic variance is greatly reduced, as the two fields sample independent large-scale structure, to a fractional cosmic variance of $\sim$ 5–8 per cent across the stellar mass range of our radio sources. The level of the cosmic variance remains similar across the full-redshift range considered in this work due to the fact that we essentially remove the lowest mass, least biased, populations as we move to higher redshifts due to the flux-density limit of the radio and multiwavelength data, whilst the comoving volume per redshift bin increases.

3 COMPLETENESS CORRECTIONS

Completeness is a key concern in constructing the luminosity function from a flux-density-limited survey. Completeness corrections become imperative for properly including faint radio sources in the analysis, where their detection is strongly correlated with the noise properties of the image. Neglecting this aspect can lead to a substantial underestimation of the space density. Furthermore, flux-density-limited surveys are susceptible to the Malmquist bias, where more luminous objects at higher redshifts and fainter objects at lower redshifts are preferentially detected. This bias introduces a potential distortion in the observed sample, leading to skewed representations of source distributions and space densities. Addressing completeness and mitigating Malmquist bias is therefore paramount for ensuring the accuracy and reliability of the derived luminosity function.

3.1 Radio completeness correction

The radio completeness quantifies the fraction of sources that are detected as a function of flux density. The noise properties of the images used in this analysis are not constant, with the noise increasing towards the edges due to the primary beam correction, so detectability varies across the field. We therefore use the results from C. L. Hale et al. (2023), who measured the completeness by injecting simulated radio sources into the residual maps and reran the source detection.

To summarize, three different input catalogues were used, based on SIMBA (R. Davé et al. 2019); SKADS (R. J. Wilman et al. 2008); and modified SKADS. These sources were injected and recovered in flux-density bins and the completeness was calculated as the ratio of the number of recovered to injected of sources in each bin. We then fit a smooth function to the binned completeness measurements using a monotonic cubic interpolation in $\log(S)$. At bright flux densities ($S > 10$ mJy), where the data are fully complete, we explicitly set the completeness to 1. The three separate simulation-based curves, shown in Fig. 2, were then combined into a single mean completeness function as a

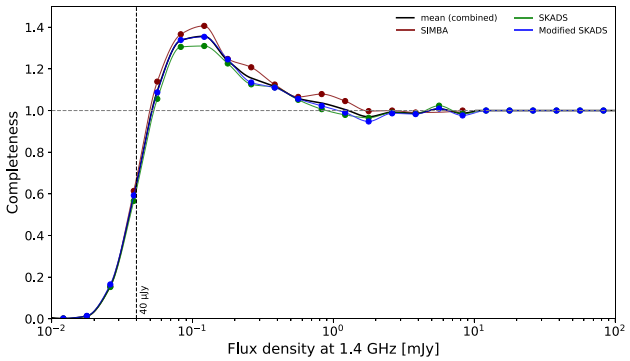

Figure 2. Completeness of the 1.4 GHz COSMOS catalogue as a function of input flux density. SKADS (green), modified SKADS (blue), SIMBA (maroon), the mean completeness is the back line. The vertical dashed line marks the uniform flux–density cut at 40 μJy; the horizontal dashed line marks 100 per cent completeness. Completeness values exceeding one intermediate flux densities result from noise shifting some sources from adjacent, lower flux bins into brighter bins (see C. L. Hale et al. 2023, for details).

function of 1.4-GHz flux density, which we apply as the radio correction in the following analysis.

In this work, we choose to use flux–density limit of $S \geq 40$ μJy, at which the completeness is 0.65. At this threshold, uncertainties associated with rms noise variations are minimized, which are more significant at lower flux-density limits and the measured flux densities become less affected by confusion noise.

3.2 Optical completeness correction

Within the unmasked area, some radio sources lack optical/NIR counterparts and thus have no redshift available, either photometric or spectroscopic. Moreover, the ancillary imaging depths differ between COSMOS and XMM–LSS, so simply discarding unmatched radio sources would bias the space densities (especially against dust-obscured and high-redshift systems) and could do so unevenly between fields. In our baseline analysis, we include these sources (hereafter referred to as non-XID) by assigning statistical redshifts. Assigning statistical redshifts to radio-only detections in each field preserves total number counts, avoids counterpart-driven selection biases, and puts both fields on a more uniform footing before combining them to determine the RLF.

To achieve this, we started with the complete radio component catalogue, which contains all detected components. Within each field we take the matched catalogue, divide it into log-spaced radio flux-density bins, and in each bin construct an empirical redshift PDF from the matched sources, smoothed with a kernel density estimator (KDE). For every unmatched radio source, we locate its flux-density bin and draw a redshift from the corresponding KDE, if that bin is empty we use the KDE from the nearest non-empty flux bin. Redshifts assigned to non-XID sources are drawn once from these flux-density dependent KDEs and are held fixed across all Monte-Carlo realizations, although we note that resampling the non-XID sources does not make any difference to our results.

In our baseline analysis, we force all sources lacking optical identifications to be at $z > 1$. Whilst approximately 50 per cent of radio sources with optical/NIR counterparts and brighter than 40μJy typically reside at $z < 1$, optically unidentified systems in this flux range are more likely to be faint galaxies that fall below the optical detection limits due to them residing at higher redshift (see e.g. F. Gentile et al. 2024, 2025). Adopting $z > 1$ for these non-XID sources therefore provides a conservative estimate of their radio luminosities and avoids biasing our analysis toward low-redshift, optically bright populations. The assigned redshifts (shown in Fig. 1) are carried forward in the analysis alongside those objects with spectroscopic or photometric redshifts.

As a check on the impact of our baseline strategy for assigning redshifts to non-XID sources, we also repeat the analysis using a second redshift assignment approach. We repeat the method of assigning redshifts to the non-XID sources, but without forcing them to be at $z > 1$. In this case, the overall redshift distribution is similar to that of the redshift distribution of sources of similar flux-density distribution, which have an optical/NIR counterparts. Adopting this strategy does not change our results significantly, as once the shape of the RLF is measured well at low redshift with a large fraction of spectroscopic redshifts, then how we spread the $\sim$ 10–15 per cent of non-XID sources does not strongly affect evolution parameters.

Finally, to check how our method of sampling from the photometric redshift PDF may affect our results, we also adopt a 'single-z' approach, in which every source is assigned a single 'best' redshift taken directly from the catalogue (spectroscopic or the best-fitting photometric redshift), rather than being sampled from its full-redshift PDF. In this approach, all non-XID sources are placed at $z > 1$, following a similar method to our baseline strategy.

The number of sources with spectroscopic and photometric redshifts in each radio luminosity and redshift bin is given in Table A1, alongside the number of non-XID sources from our baseline model where they are forced to have $z > 1$.

4 THE RADIO LUMINOSITY FUNCTION

In this section, we describe the form of the radio luminosity function (RLF) that we adopt in this analysis, how we calculate the RLF in redshift bins, and how we model its evolution.

4.1 The $1/V_{max}$ method

To measure the cosmic evolution of radio sources, we determine the RLFs for different redshift bins using the $1/V_{\rm max}$ method (M. Schmidt 1968).

We first calculate the rest-frame radio luminosity at 1.4 GHz, corresponding to the observed-frame flux density. The MIGHTEE data has a varying effective frequency across the image, with a mean effective frequency of $\nu_{\rm eff} \sim 1.28$ GHz. To determine the rest-frame luminosity at 1.4 GHz ($L_{1.4_{\rm rf}}$) we therefore use,

$$L_{1.4_{\rm rf}} = \frac{4\pi D_L^2}{(1+z)^{1+\alpha}} S_{\nu_{\rm eff}} \left(\frac{1.4}{\nu_{\rm eff}}\right)^{\alpha}, \quad (1)$$

where D_L is the luminosity distance, α is the spectral index of the source[1] and z is the redshift of the source. In practice, we use the effective frequency associated with the position of the source in the continuum images as described in I. Heywood et al. (2022). The rest-frame 1.4 GHz luminosity as a function of redshift for our sample is shown in Fig. 3 for both the COSMOS and XMM–LSS fields.

[1]We assume $\alpha = -0.7$, which is typical for SFGs (J. J. Condon 1992b; E. F. Bell 2003)

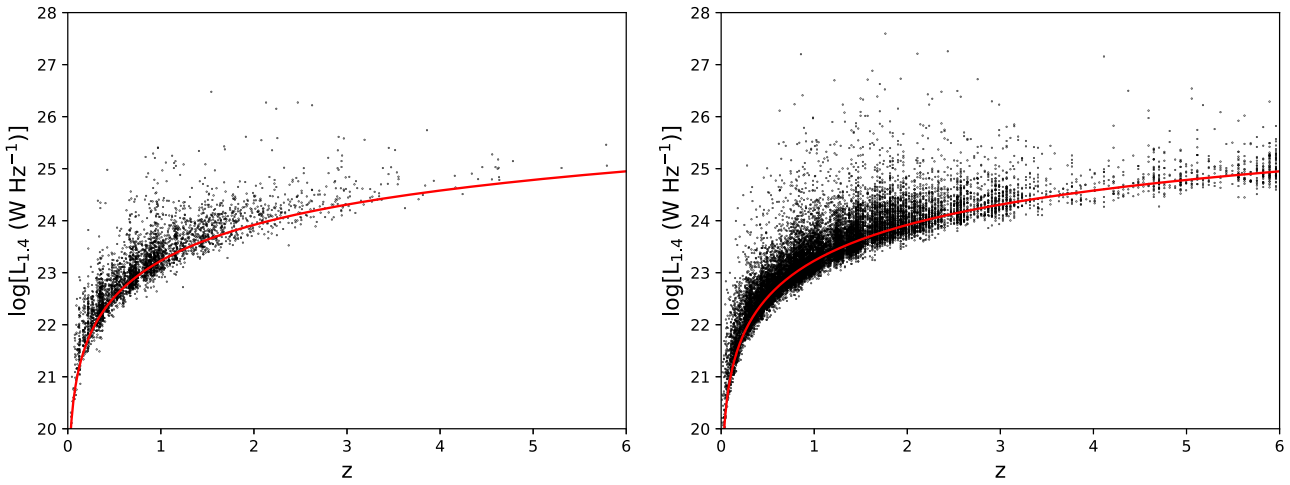

Figure 3. Rest-frame 1.4 GHz luminosity versus redshift for COSMOS (left) and XMM–LSS (right). Black points are individual sources. The solid red curve corresponds to the adopted 40 μJy flux-density cut at the frequency.

The radio luminosity function (number density per unit $\log L$) is given by

$$\phi(L, z) = \frac{1}{\Delta \log L} \sum_{i=1}^{N} \frac{1}{V_{\mathrm{max_i}}}, \tag{2}$$

with the corresponding uncertainty given by H. L. Marshall (1985):

$$\sigma_{\phi(L,z)} = \frac{1}{\Delta \log L} \sqrt{\sum_{i=1}^{N} \frac{1}{V_{\mathrm{max_i}}^2}}, \tag{3}$$

where $V_{\mathrm{max},i}$ is the maximum comoving volume accessible to source i in the given (L, z) bin.

We calculate V_{max} by dividing the sample into ten redshift bins spanning $0.2 < z < 4.6$. We limit the analysis to $z > 0.2$ as we do not have the necessary cosmic volume to accurately measure the luminosity function at $z < 0.2$. We adopt a luminosity–bin width of $\Delta \log L = 0.25$ dex to strike a balance of preserving useful resolution across a reasonable range in luminosity while limiting the Poisson noise, and limiting leakage between adjacent bins due to photometric redshift uncertainties and noise fluctuations. At the bright end, where sources are sparse, we widen to $\Delta \log L = 0.4$ for $\log L \geq 26$ to compensate for the low source density.

For each source i, V_{max} is computed by summing the accessible comoving volume element within each redshift bin from z_{min} to z_{max}, where z_{max} is set by the redshift at which the observed flux density at 1.4 GHz drops to the survey selection limit ($S_{1.4} \geq 40$ μJy), and is capped at the upper edge of the relevant redshift bin. We also apply a completeness correction $C(S_{1.4})$ using the empirical completeness curves shown in Fig. 2, to obtain a completeness corrected measurement of the maximum accessible comoving volume for each source:

$$V_{\mathrm{max},i} = \sum_{z=z_{\mathrm{min}}}^{z_{\mathrm{max}}} \left[V(z + \Delta z) - V(z) \right] C(S_{1.4}). \tag{4}$$

The incompleteness due to some radio sources lacking an optical/NIR counterpart is, as described in Section 3.2, accounted for by including unmatched sources with statistical redshift values.

4.2 Parametrization of the radio luminosity function

To quantify the combined RLF for both AGN and SFGs, we consider the parametric forms used in previous work. Specifically, we adopt a double power law for the AGN, following T. Mauch & E. M. Sadler (2007):

$$\phi_0^{\mathrm{AGN}}(L) = \frac{\phi_*^{\mathrm{AGN}}}{\left(\frac{L}{L_*^{\mathrm{AGN}}}\right)^a + \left(\frac{L}{L_*^{\mathrm{AGN}}}\right)^b} \tag{5}$$

where ϕ_*^{AGN} is the normalisation, L_*^{AGN} is the knee or break in the RLF, and a and b are the bright- and faint-end slopes.

For the SFG population, we use the four parameter analytical form used by M. Novak et al. (2017), which is comprised of a power-law plus lognormal distribution from W. Saunders et al. (1990):

$$\phi_0^{\mathrm{SF}}(L) = \phi_*^{\mathrm{SF}} \left(\frac{L}{L_*^{\mathrm{SF}}}\right)^{1-\delta} \exp\left[-\frac{1}{2\sigma^2} \log^2\left(1 + \frac{L}{L_*^{\mathrm{SF}}}\right)\right], \tag{6}$$

where ϕ_*^{SF} is the normalisation, L_*^{SF} is the knee of the distribution, δ is the faint-end slope and σ describes the exponential fall off beyond the knee.

Both the AGN and SFG populations are known to evolve strongly with redshift. This evolution is traditionally modelled as either; (i) pure luminosity evolution, whereby the specific population changes in luminosity with redshift, and the comoving space density of the population remains constant; (ii) pure density evolution, where the comoving space density evolves with redshift; or (iii) a combination of both of these evolutionary forms. In practice, the data are often not sufficient to fully disentangle pure luminosity from pure density evolution or combinations thereof, as the data need to sample below and above the knee or break in the luminosity function. This means that both deep and wide areas are necessary. This is particularly true for radio surveys, where we have a combination of both SFGs and AGN, which have different shaped luminosity functions and may evolve in different ways.

For this study, we adopt an approach driven by our core science aims, to measure the evolution of the SFGs using the radio continuum data, whilst accounting for the contribution to the total radio luminosity function from the AGN. We therefore fix the shape

of the AGN luminosity function using the local AGN luminosity function from M. Novak et al. (2018), which is consistent with T. Mauch & E. M. Sadler (2007). We allow the AGN luminosity function to evolve using a pure density-only evolution model, due to the fact that we do not have enough cosmological volume to accurately determine the break of the AGN part of the RLF, which is important for decoupling pure density from pure luminosity evolution. We note that our results for the SFG luminosity function do not change significantly if we adopt a pure luminosity evolution model for the AGN. We parametrize the evolution with,

$$\phi(\mathrm{AGN}) = \phi_0^{\mathrm{AGN}}(1+z)^{\alpha_D^{\mathrm{AGN}}+z\beta_D^{\mathrm{AGN}}}, \tag{7}$$

where α_D^{AGN} and β_D^{AGN} provide the flexibility to model the expected increase in comoving space density from low to high redshift, whilst also permitting a turnover beyond a given redshift.

For the SFGs, which are the focus of this work, we allow all the parameters of the local luminosity function (equation 6) to be free parameters, and adopt a pure luminosity evolution model, due to the fact that we predominantly sample beyond the knee in the luminosity function, given by

$$\phi(\mathrm{SF}) = \phi_0^{\mathrm{SF}}\left[\frac{L}{(1+z)^{\alpha_L^{\mathrm{SF}}+z\beta_L^{\mathrm{SF}}}}\right], \tag{8}$$

where α_L^{SF} and β_L^{SF} again provide flexibility for the luminosity evolution to increase and then decrease beyond a given redshift.

We then fit for both the AGN evolution parameters (α_D^{AGN} and β_D^{AGN}) and the SFG evolution parameters (α_L^{SF} and β_L^{SF}) along with the overall shape of the SFG RLF, similar to K. McAlpine et al. (2013). One advantage of fitting the total RLF is that the inference does not depend on the specific galaxy classification scheme, provided the RLF shapes for the SFG and AGN populations are adequately specified.

4.3 Multinest sampling

To explore the multiparameter likelihood space, in order to find the best-fitting RLF parameters and associated posteriors, we use MULTINEST (F. Feroz & M. P. Hobson 2008). MULTINEST is a Bayesian inference algorithm designed to efficiently calculate the Bayesian evidence and explore complex parameter spaces. MULTINEST returns the full posterior distribution, enabling robust parameter estimation and accurate uncertainty quantification. We use the Python interface PYMULTINEST (J. Buchner et al. 2014).

In Bayesian inference, we seek the posterior

$$P(\boldsymbol{\theta}\,|\,D,H) = \frac{\mathcal{L}(D\,|\,\boldsymbol{\theta},H)\,\pi(\boldsymbol{\theta}\,|\,H)}{Z(D\,|\,H)}, \tag{9}$$

where $\boldsymbol{\theta}$ are the model parameters, D the data, H the model, $\mathcal{L}$ the likelihood, and π the prior. The Bayesian evidence (z) given by

$$Z(D\,|\,H) = \int \mathcal{L}(D\,|\,\boldsymbol{\theta},H)\,\pi(\boldsymbol{\theta}\,|\,H)\,\mathrm{d}\boldsymbol{\theta} \tag{10}$$

normalises the posterior and enables quantitative model comparison.

We adopt uniform priors with bounds set by physical plausibility on all local–SFG luminosity function and all evolution parameters (Table 1), apart from L_*^{SF} and ϕ_*^{SF}, where we adopt lognormal priors centred around the local values given by M. Novak et al. (2017). This is because our survey has limited volume at low redshift and both the normalisation and knee in the luminosity function are relatively well-defined at low redshift. As we fit for the faint-end slope it also removes some of the degeneracy whilst retaining the flexibility for a flatter or steeper faint-end slope for the SFG luminosity function. We marginalize over the photometric–redshift uncertainty via a per–resample Monte–Carlo strategy. For each of $N_{\mathrm{rep}} = 100$ realizations (where N_{rep} is the number of photometric–redshift resampling iterations), the redshift of every source is sampled from the PDF of its photometric redshift, while spectroscopic redshifts and non-XID values are kept fixed. The full binned RLF across all redshifts is recomputed, and a single MULTINEST fit is run to obtain posterior samples for each realization. The final photometric redshift posterior is formed by equal weight concatenation of the posterior samples from all N_{rep} runs. This numerically integrates over the photometric redshift PDFs without reweighting and preserves the correct overall likelihood weight.

Table 1. Priors adopted for the free parameters in the model fitting. Lognormal priors are assumed for the local SFG RLF parameters ϕ_*^{SF} and L_*^{SF}, and uniform priors are adopted for the remaining RLF parameters. The local AGN RLF parameters are held fixed in all fits (see Table 2).

Parameters	Priors
$\log(\phi_*^{\mathrm{SF}}/\mathrm{Mpc}^{-3}\,\mathrm{dex}^{-1})$	Gaussian $\sim(\mu=-2.45,\ \sigma=0.30)$
$\log(L_*^{\mathrm{SF}}/\mathrm{W\,Hz}^{-1})$	Gaussian $\sim(\mu=21.25,\ \sigma=0.25)$
δ	Uniform $\in[-2,5]$
σ	Uniform $\in[0,1]$
α_L^{SF}	Uniform $\in[0,5]$
β_L^{SF}	Uniform $\in[-1,0]$
α_D^{AGN}	Uniform $\in[0,5]$
β_D^{AGN}	Uniform $\in[-2,0]$

5 RESULTS AND DISCUSSION

In Fig. 4, we present the total RLF in redshift bins, showing our $1/V_{\mathrm{max}}$ measurements and the modelled redshift evolution of the SFG and AGN components alongside data points from previous studies. The corresponding posterior distributions of the model parameters for the case where we distribute non-XID radio sources at $z>1$ are shown in Fig. 5. For the other approaches, the total RLFs and the corresponding corner plots are shown in Figs B1 and B2 (uniform-z for non-XID sources) and Figs B4 and B5 for the case of a single best redshift.

5.1 The local radio luminosity function of SFGs

The first thing that is noticeable with our measured binned luminosity function values (Fig. 4) is that at low redshift and at the lowest luminosities they are significantly higher than the luminosity function point from M. Novak et al. (2017), who use data from the 3 GHz survey over the COSMOS field. However, our data are consistent with the other very deep MeerKAT survey over the DEEP2 field by A. M. Matthews et al. (2024). The key differences between the VLA-3GHz survey and both ours and the DEEP2 MeerKAT data are the observed frequency ($\sim$ 1.3 GHz vs 3 GHz), but probably more importantly is the sensitivity of MeerKAT to low-surface brightness emission. The latter is likely the more important consideration, as many studies have shown that the spectral index distribution between 1.4 and 3 GHz is well behaved with a mean spectral index of $\alpha \approx 0.7$. Indeed, C. L.

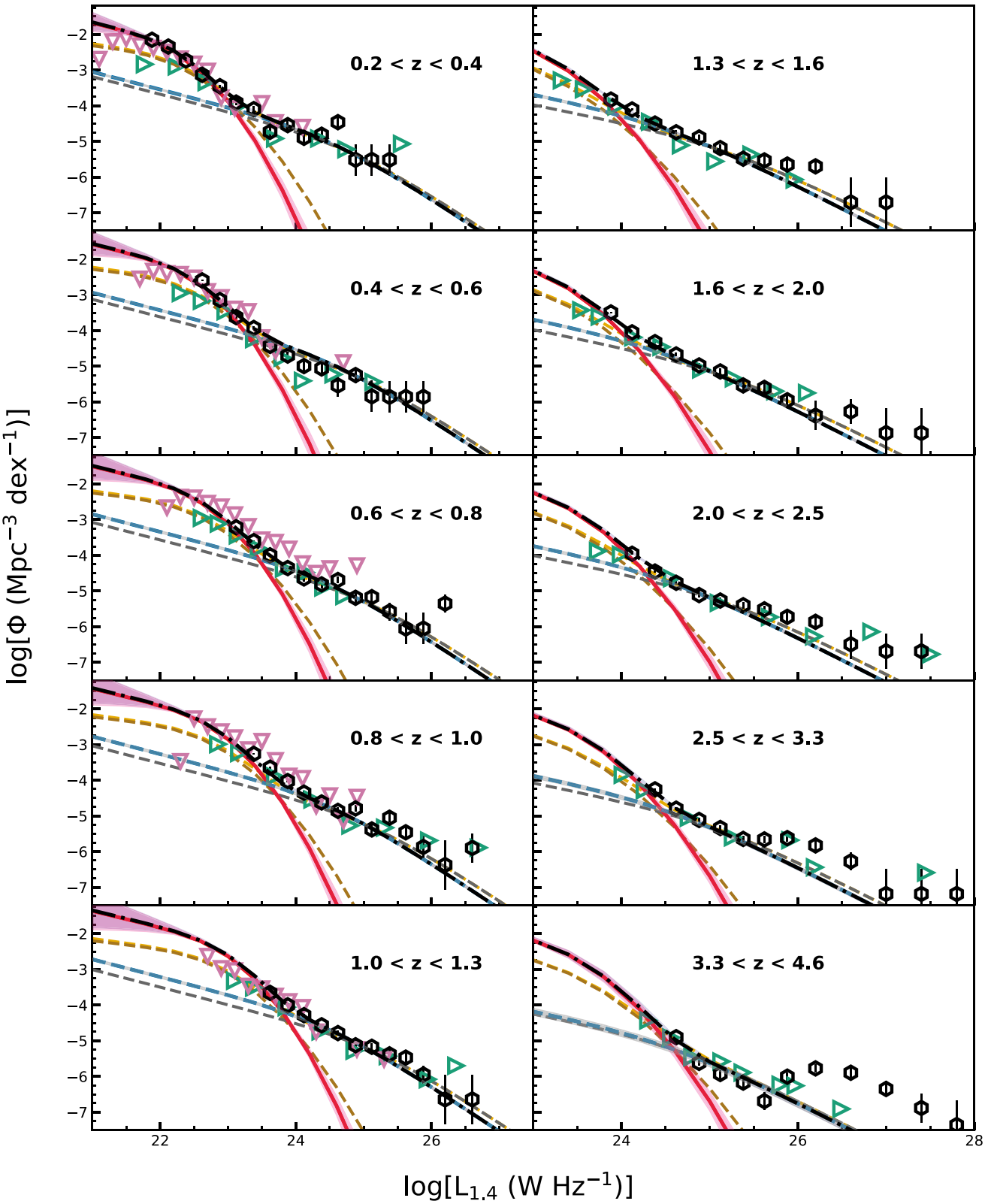

Figure 4. Total 1.4 GHz RLF in ten redshift bins from our photometric redshift PDF-based analysis, including statistically assigned redshifts for the non-XID sources restricted to be at $z > 1$. Black hexagons show the $1/V_{\rm max}$ measurements from this work. Red solid and blue dashed curves show the best-fitting SF (PLE) and AGN (PDE) components, respectively, with magenta and light-blue bands show their 90 per cent confidence intervals. The combined total LF is shown as a black dash–dotted curve. The yellow, brown and grey dashed curves denote the total, SFG, and AGN RLFs, respectively, from M. Novak et al. (2018). For reference, the $1/V_{\rm max}$ points from M. Novak et al. (2018) and A. M. Matthews et al. (2024) are also shown as green right-pointing and magenta down-pointing triangles, respectively.

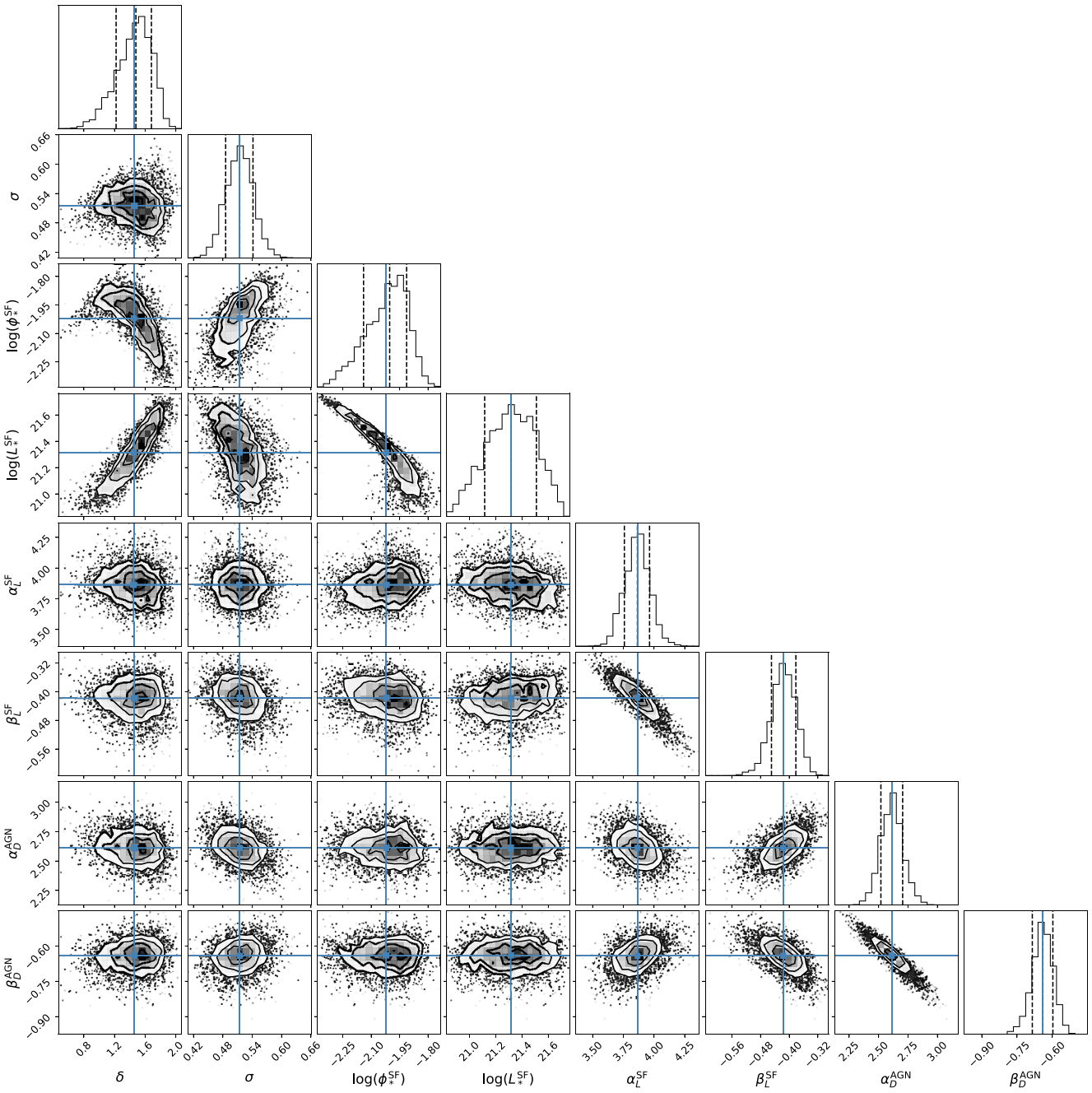

Figure 5. Posterior distributions for the eight parameters of the total RLF model: SFG Schechter function parameters (δ, σ, $\phi_*^{\rm SF}$, $L_*^{\rm SF}$), SFG luminosity evolution ($\alpha_L^{\rm SF}$, $\beta_L^{\rm SF}$), and AGN density evolution ($\alpha_D^{\rm AGN}$, $\beta_D^{\rm AGN}$). Contours show the 68th and 95th percentile confidence regions; vertical lines in the 1D marginals mark the median and 16th/84th percentiles. The SFG (PLE) and AGN (PDE) evolution pairs exhibit the expected anticorrelations, while cross-component couplings remain weak, indicating that the two channels are separately constrained.

Hale et al. (2023) showed that the MIGHTEE data detected lower surface brightness, but relatively high flux density ($\gtrsim 100\,\mu$Jy), sources that were completely invisible in the VLA-3GHz survey data, even though the flux-density sensitivity would suggest that such objects should have been detected at $> 50\sigma$. This is due to the core-dominated baseline distribution of the MeerKAT array, which results in both high sensitivity to diffuse emission, coupled with long enough baselines to image at ~ 5 arcsec resolution. On the other hand, the VLA-3GHz survey was designed to maximise resolution using the VLA A-Array configuration to allow more robust cross-identification to optical counterparts and enabling studies of the radio morphology to help separate AGN from SFGs. However, this survey design comes at the cost of losing low-surface brightness sensitivity due to the absence of high enough sensitivity on short baselines. Although the VLA-3GHz survey complemented the A-array data with shallower C-array data, this clearly was insufficient to detect the faint low-surface brightness emission that is seen with MeerKAT. All of this essentially leads to both more low-surface brightness galaxies being detected for a given total flux density and more emission being detected for

galaxies already in the sample, thus moving them to higher radio luminosities, in the MeerKAT data.

Another difference between the MIGHTEE data used here, particular in the COSMOS field, and the VLA-3GHz work of M. Novak et al. (2017), is the availability of many more spectroscopic redshifts since 2017 (see Table A1), particularly in these low-redshift bins, from DESI (DESI Collaboration 2024). This means that our measured luminosity function is more robust at these redshifts and luminosities. Thus, the significantly higher normalisation at the faint end is indeed real, providing confirmation of similar results using MeerKAT data (A. M. Matthews et al. 2024).

As the faint-end slope of the measured RLF is constrained primarily by the lowest redshift bin, we compare our $0.2 < z < 0.4$ RLF to the NVSS-based local 1.4 GHz RLF of T. Mauch & E. M. Sadler (2007). We find a similar exponential drop beyond the knee of the RLF for SFGs, however, we find a significantly steeper faint-end slope, with T. Mauch & E. M. Sadler (2007) finding $\delta = 1.02$ compared to our value of $\delta = 1.48$. Although consistent at the 2σ level, the difference is also likely due to the relatively bright $K-$band magnitude limit coupled with the strong correlation between radio luminosity and $K-$band magnitude which leads to some incompleteness at the lowest radio luminosities in the local study of T. Mauch & E. M. Sadler (2007).

The other noticeable aspect in our measured luminosity functions is the upturn towards higher luminosities that is due to the contribution of the AGN, i.e. the total RLF is a combination of two underlying distributions of two different populations, where the radio emission is related to different physical processes. Indeed, this is the reason we choose to model the total RLF as described in Section 4.2.

The observed higher normalisation of the low-luminosity end of the RLF clearly leads to a different best-fitting functional form for the local radio luminosity function of SFGs, compared to M. Novak et al. (2017), which is the closest study in terms of depth and frequency, albeit with smaller area. We find a value of $\delta = 1.48^{+0.20}_{-0.26}$ for the faint-end slope of the SFG luminosity function. This value is steeper than the faint-end slope measured for local RLF of SFGs found by M. Novak et al. (2017) of $\delta = 1.22$, although we note that they are formally consistent within the uncertainties. However, such a steep slope is consistent with the faint-end slope of the luminosity function at other wavelengths. For example, the ultraviolet luminosity function at low-redshift (S. Arnouts et al. 2005) has a slope of $-1.5 < \delta < -1.2$. At FIR wavelengths M. P. Koprowski et al. (2017) find a similar value of $\delta = -1.4$ (converting their definition of δ to that used from equation (6)). We also note that in fig. 3 of M. Novak et al. (2017) the data points at low luminosity generally sit above their model faint-end slope and it is only the final points in each sample, where the completeness corrections are the most significant, that force the faint-end slope to be flatter than what we find here.

However, this steeper slope is also coupled with a significantly higher normalisation term $\log(\phi_*^{\rm SF}/\ {\rm Mpc}^{-3}\,{\rm dex}^{-1}) = -2.00^{+0.10}_{-0.11}$, compared to $\log(\phi_*^{\rm SF}/\ {\rm Mpc}^{-3}\,{\rm dex}^{-1}) = -2.45$ in M. Novak et al. (2017), even with a lognormal prior set around the latter value. Together, these provide a best-fitting model that suggests there is a far greater number of SFGs in deep radio surveys than inferred from previous surveys that cannot detect the low-surface brightness diffuse emission. However, although the best-fitting local luminosity function parameters for the SFG population are robust, Fig. 5 shows that δ, $\phi_*^{\rm SF}$ and $L_*^{\rm SF}$ are highly degenerate. This is a well-known aspect of the functional form adopted, and emphasizes the requirement to have a robust measurement of the luminosity function both above and below the knee. Indeed, this is the reason we fix the AGN-related part of the luminosity function to the local values.

5.2 The evolution of the SFG and AGN luminosity function

We next turn to the best-fitting to the evolutionary parameters: $\alpha_L^{\rm SF}$ and $\beta_L^{\rm SF}$ for the pure luminosity evolution of the SFGs and $\alpha_D^{\rm AGN}$ and $\beta_D^{\rm AGN}$ for the pure density evolution of the AGN. We find evidence for strong evolution of the SFG luminosity function, with $\alpha_L^{\rm SF} = 4.0$ with a shallow but significant turnover at high redshifts with $\beta_L^{\rm SF} = -0.42$ (for both cases of redistributing the non-XID radio sources). The strength of this evolution means that the comoving space density of SFGs increases by a factor of ~ 10 from $z \sim 0 \rightarrow 2$. This evolution is similar in magnitude to that found at other wavelengths for SFGs, providing independent evidence that the combined SFG and AGN luminosity functions used in this work are behaving as one would expect in terms of their evolution. However, due to the fact that the normalisation of the local luminosity function in this work has a much higher value, coupled with a steep faint-end slope, we also obtain a significantly higher comoving space density at high redshift. This is largely due to the adoption of pure luminosity evolution and a faint-end slope and normalisation fixed by the low-redshift data. However, we also note that a pure-density evolution model produces a similar degree of evolution due to the need to fit the bright end of the SFG luminosity function at higher redshifts. We return to the implications of this for the evolution of the cosmic SFRD in Section 5.3.

For AGN, the PDE fit ($\alpha_D^{\rm AGN}$, $\beta_D^{\rm AGN}$) produces a vertical shift in normalisation while keeping the RLF shape fixed. The comoving space density of AGN also rises from $z = 0$ to $z \sim$ 1-2 and then flattens, in agreement with previous deep radio surveys (K. McAlpine et al. 2013; V. Smolčić et al. 2017b). The posterior distributions (Fig. 5) show the expected anticorrelations within $\alpha_L^{\rm SF}$, $\beta_L^{\rm SF}$ and $\alpha_D^{\rm AGN}$, $\beta_D^{\rm AGN}$, with relatively weak cross-component couplings between the AGN and SFG luminosity functions, indicating that PLE (SFG) and PDE (AGN) are independently constrained.

These results support the adopted modelling choice of PLE for SFG and PDE for AGN. Our data do not bracket the break in the RLF for AGN ($L_*^{\rm AGN}$) in most redshift bins, so the AGN LF is effectively single power–law over the luminosity range we probe; allowing the AGN shape to shift would be weakly constrained and largely degenerate with normalisation. Fixing the AGN shape and evolving only its density thus captures what the data measure most directly. In contrast, the SFG constraints are strongest near the bright-end of the SFG RLF, so a horizontal shift in L_*^{SF} is well measured and physically interpretable as the movement of the knee in the SFG RLF to higher luminosities with increasing redshift.

The single-redshift analysis (Fig. B4), which assigns each source a single best redshift, likewise agrees with the $z > 1$ results in overall shape and amplitude. Differences arise in the sparsest, highest-redshift bins and at the brightest luminosities, where the absence of smoothing over the photometric redshift PDFs can accentuate Poisson spikes. Refitting under the different treatments produces small, compensating shifts in local RLF parameters (e.g. $\phi_*^{\rm SF}$, $L_*^{\rm SF}$). Quantitatively, inferred evolutionary trends are statistically unchanged and the SFG/AGN separation

remains consistent across redshift; any deviations are limited to minor shifts in a few $1/V_{\rm max}$ points at the highest luminosities.

5.3 Star formation rate density

The functional form of the evolving SFG luminosity function allows us to measure the evolution in the comoving SFRD of the Universe, assuming the radio luminosity for these sources closely traces the SFR. The link between SFR and radio luminosity has been extensively studied at both low and high redshifts. Traditionally this has been done through the use of the radio–FIR correlation (e.g. G. Helou, B. T. Soifer & M. Rowan-Robinson 1985; M. S. Yun et al. 2001; E. F. Bell 2003; M. J. Jarvis et al. 2010; J. Delhaize et al. 2017). However, more recent studies have used full spectral energy distribution modelling to determine the SFR from all components of a galaxy SED (e.g. L. J. M. Davies et al. 2017; G. Gürkan et al. 2018; D. J. B. Smith et al. 2021a; R. H. W. Cook et al. 2024).

Here we derive the SFRD by integrating our RLFs in redshift slices. For the radio–to–SFR conversion we use two tracks, an evolving FIR–radio correlation (evolving–q) following J. Delhaize et al. (2017) and M. Novak et al. (2017), and a non-evolving (fixed–q) control (with a constant FIR–radio correlation) from E. J. Murphy (2009). Using two separate evolution models is valuable as they give an indication of the range of plausible SFRs derived from the FIR–radio correlation for the SFGs in our sample and the associated RLF.

For our evolving-q track, we adopt the relation from M. Novak et al. (2017):

$$q_{\rm TIR}(z) = 2.78\,(1+z)^{-0.14}, \tag{11}$$

$$\mathrm{SFR}_{\text{evolving-q}} = f_{\rm IMF}\,10^{-24}\,10^{q_{\rm TIR}(z)}\,\frac{L_{1.4}}{\mathrm{W\,Hz^{-1}}}, \tag{12}$$

where $f_{\rm IMF}$ is the IMF normalisation factor (set to 1 for a Chabrier IMF), and $L_{1.4}$ is the rest-frame 1.4 GHz luminosity. This evolving $q_{\rm TIR}$ allows for the observed decline of $q_{\rm IR}$ with redshift, plausibly tied to a stellar mass dependence coupled with a flux-limited sample at near-infrared wavelengths (I. Delvecchio et al. 2021; D. J. B. Smith et al. 2021a).

The cosmic SFRD is then given by

$$\mathrm{SFRD}(z) \;=\; \int_{L_{\rm min}}^{L_{\rm max}} \phi_{\rm SF}(L,z)\,\mathrm{SFR}(L,z)\,\mathrm{d}\log L, \tag{13}$$

where $\phi_{\rm SF}(L,z)$ is the SFG RLF. For consistency across redshift bins, we integrate in log-space from $\log(L_{\rm min}) = 20.0$ to $\log(L_{\rm max}) = 26.1$, noting that the bulk of the luminosity density arises from near the knee of the RLF and the exact choice of these limits does not affect the overall results.

Fig. 6 shows both the fixed-q (red-dashed) and evolving-q (blue-dashed) curves derived using the same RLF fit, their separation reflects only the calibration used to convert to SFR. Both calibrations are informative, the evolving-q curve provides a baseline that accounts for the observed decline of $q_{\rm TIR}(z)$, whereas the fixed-q curve offers continuity with much of the historical radio literature and serves as a transparent control. Together they bracket the radio-to-SFR calibration uncertainty based on the FIR–radio correlation. In both cases, the radio-derived SFRD rises to $z\sim2$ and then declines at earlier epochs as expected from a range of multiwavelength studies (e.g. P. Madau & M. Dickinson 2014). However, the radio-derived SFRDs from our measured RLF for SFGs are consistently higher than UV + IR compilations, especially below $z\sim1.3$, where we have the strongest constraints. Given the very high spectroscopic completeness at the lowest redshifts in our sample (see Table A1), this cannot be attributed to photometric redshift uncertainties. Indeed, we have almost 100 per cent spectroscopic redshifts for our lowest redshift bin in the COSMOS field and find that the normalisation is consistent between COSMOS and the XMM–LSS field. Therefore, we are finding a genuinely higher luminosity function normalisation. Once this form of the luminosity function is set by the low-redshift points, then it is inevitable that the SFRD remains consistently high across all redshifts, as the overall shape of the RLF is retained across all redshifts.

This higher normalisation has also been found by a comparable study using MeerKAT data over the DEEP2 field by A. M. Matthews et al. (2024) and to a lesser degree in other recent deep radio survey (e.g. A. Enia et al. 2022; R. K. Cochrane et al. 2023). Indeed, our analysis confirms the results of A. M. Matthews et al. (2024), where they acknowledge the limitations of their single-deep-field survey, which increases the uncertainty in the normalisation due to cosmic variance, which is of the order of 20 per cent in the lowest redshift bins. Given we have two separate fields, which we would not expect to be at all correlated in the large-scale structure they contain, the cosmic variance across the two fields (noting the larger area in XMM–LSS) should therefore be reduced by a factor of ~ 2 (see equation 9 in B. P. Moster et al. 2011). Thus, cosmic variance cannot explain the factor of ~ 2 higher SFRD in the radio compared to the other multiwavelength tracers.

We overplot the radio-only SFRD model of A. M. Matthews et al. (2021) in Fig. 6. The model constrains the redshift evolution of the SFRD statistically by fitting the 1.4 GHz source counts, without requiring individual redshifts. The resulting track lies between our fixed–q and evolving–q curves and shares the same broad rise and decline with redshift, supporting the view that our photometric-redshift PDF–based RLF modelling is fully consistent with earlier counts–based constraints on the radio SFRD from MeerKAT observations, and that the elevated radio normalisation is unlikely to be driven by redshift incompleteness or photometric–redshift systematics.

The most likely explanation is the conversion used to determine the galaxy SFR from the radio luminosity. Although we use the standard relation from E. J. Murphy et al. (2011), this relation is derived solely from FIR data. Using the MIGHTEE survey data, R. H. W. Cook et al. (2024) derived SFRs for all the MIGHTEE radio continuum galaxies using full SED modelling of the UV-far-infrared data. They found a slightly shallower relation between radio luminosity and SFR of the form:

$$\mathrm{SFR/M_\odot\,yr^{-1}} = 10^{1.014\pm0.003}\left(\frac{L_{1.4}}{5\times10^{22}\,\mathrm{WHz^{-1}}}\right)^{0.868\pm0.005}. \tag{14}$$

For a similar evolving q to that described by J. Delhaize et al. (2017) and M. Novak et al. (2017), this leads to

$$q_{\rm tot}(z) = 5.31(1+z)^{-0.14}, \tag{15}$$

where, in this case $q_{\rm tot}$ denotes the evolving relation between SFR and 1.4 GHz luminosity defined using the R. H. W. Cook et al. (2024) relation at $z = 0$. This then leads to an alternative evolutionary form:

$$\mathrm{SFR}_{q_{\rm tot}}/\mathrm{M_\odot\,yr^{-1}} = f_{\rm IMF}\,10^{-24}\,10^{q_{\rm tot}(z)}\left(\frac{L_{1.4}}{\mathrm{W\,Hz^{-1}}}\right)^{0.868}. \tag{16}$$

The evolution of the SFRD shown by the lines labelled 'SED-derived' in Fig. 6 use this calibration. This relation results in lower overall SFRs for a given radio luminosity compared to equations

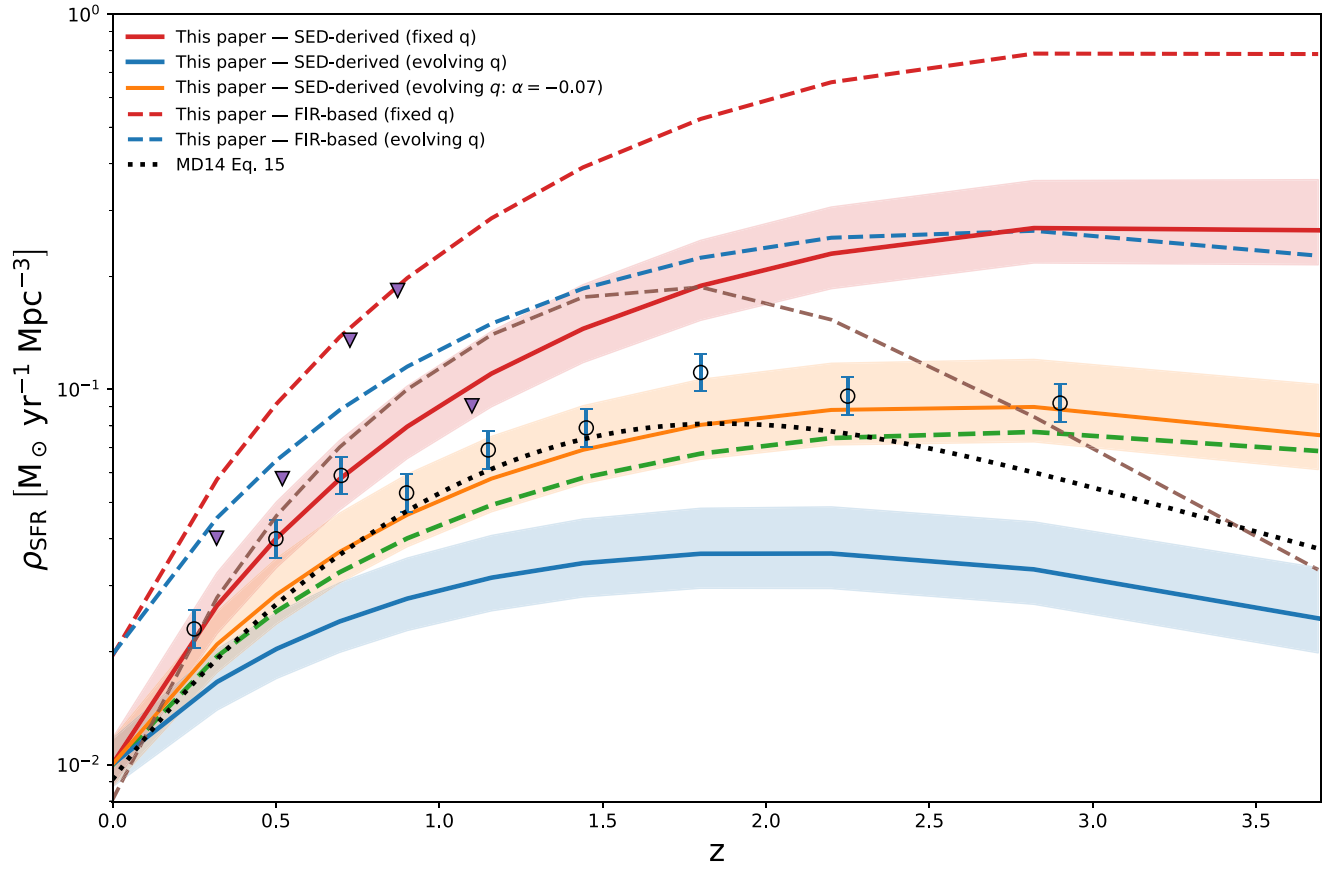

Figure 6. SFRD, $\rho_{\rm SFR}$, as a function of redshift. Solid lines show the evolution assuming the SED-derived conversion to SFR from radio luminosity (R. H. W. Cook et al. 2024). The fixed-q track is denoted by the red curve (with 68 per cent confidence band) and the evolving-q track by the blue line (with 68 per cent confidence band). We also show an alternative line with $q_{\rm tot} \propto (1+z)^{-0.07}$ (orange). For comparison, the dashed lines show the SFRD based on the FIR-based conversion from radio luminosity to SFR with fixed-q (red) and evolving-q (blue). The brown dashed curve shows the radio-only model from A. M. Matthews et al. (2021). We also show data points from radio-derived SFRD measurements from various literature: M. Novak et al. (2017) (green dashed line), R. K. Cochrane et al. (2023) (open circles with blue error bars) and A. M. Matthews et al. (2024) (purple inverted triangles). The black dotted line is the UV + IR compilation fit of P. Madau & M. Dickinson (2014). We only show the confidence region for our baseline model for clarity.

(11) and (12). Indeed, the difference in SFR at the knee of the luminosity function at $L_*^{\rm SF} = 10^{21.32}$ W Hz^{-1} where the bulk of the SFRD arises, is a factor of 1.8, which can account for the factor of ~ 2 higher normalisation in the low-redshift SFRD. Fig. 6 demonstrates this, and also largely reconciles the apparent discrepancy between previous work on the SFRD derived from deep radio data compared to UV and FIR data.

We also show how adopting the relationship between SFR and radio luminosity from R. H. W. Cook et al. (2024), alongside a non-evolving dependence of this relation with redshift (red line in Fig. 6), which shows excellent agreement with the similar study by R. K. Cochrane et al. (2023) using deep LOFAR data, at least out to $z \sim 1$.

However, it should also be noted that the closer agreement between the SFRD based on the R. H. W. Cook et al. (2024) relation and the UV + FIR derived SFRD from P. Madau & M. Dickinson (2014), is inevitable to a certain degree, and not based on a deeper understanding of the physical processes involved. By insisting that the SFR derived from radio luminosity is tied to SFR derived from the full SED fitting, we should obtain the same normalisation in the SFRD as one would obtain from using the UV–FIR data, assuming that both samples are complete to a given SFR. This highlights the importance of using the correct relation between radio luminosity and SFR, but also highlights that when enforcing consistency at the lowest redshifts then we find that the radio-derived evolving SFRD closely matches that of the dust-corrected SFRD (P. Madau & M. Dickinson 2014).

Beyond $z \sim 1$, the non-evolving model using equation (14) generally overpredicts the SFRD compared to the UV- and FIR tracers. On the other hand incorporating a similar redshift dependence to that of M. Novak et al. (2017) (equation (16)) appears to underpredict the SFRD, although field-to-field variations and cosmic variance may account for some of this discrepancy. However, this may also be resolved by considering the mass-dependence of the SFR–radio luminosity relation (e.g. G. Gürkan et al. 2018; I. Delvecchio et al. 2021; D. J. B. Smith et al. 2021a) or by adopting a shallower redshift evolution in equation (11), consistent with the lack of significant evolution in the radio–SFR relation at $1.5 < z < 3.5$ reported by F. Tabatabaei et al. (2025), also using MIGHTEE data. For illustration, in Fig. 6, we also show a line for $q_{\rm tot} \propto (1+z)^{-0.07}$ highlighting the sensitivity of the high-redshift SFRD to the form of the evolution, especially for a non-linear relationship between SFR and radio luminosity.

Table 2. Best-fitting parameters for RLF of SFGs and AGN. We show the results using the two different approaches of assigning redshift statistically for those sources without an optical/NIR counterpart (non-XID), with those restricted to be at $z > 1$ shown in the first row, with row 2 showing the results when the non-XID sources are allowed to populate all redshift ranges. The third column shows the results when the best-fitting photometric redshift is used for those sources without a spectroscopic redshift. We fit a pure luminosity evolution (PLE) model for SFGs ($\alpha_L^{\rm SF}$, $\beta_L^{\rm SF}$) and a pure density evolution (PDE) model for AGN ($\alpha_D^{\rm AGN}$, $\beta_D^{\rm AGN}$). The local AGN LF parameters were fixed: $\log(\phi_*^{\rm AGN}/{\rm Mpc^{-3}\,dex^{-1}}) = -5.1$, $\log(L_*^{\rm AGN}/{\rm W\,Hz^{-1}}) = 24.59$, $a = -1.27$ and $b = -0.49$.

Method	$\log(\phi_*^{\rm SF}/{\rm Mpc^{-3}\,dex^{-1}})$	$\log(L_*^{\rm SF}/{\rm W\,Hz^{-1}})$	δ	σ	$\alpha_L^{\rm SF}$	$\beta_L^{\rm SF}$	$\alpha_D^{\rm AGN}$	$\beta_D^{\rm AGN}$
$z > 1$	$-2.00^{+0.10}_{-0.11}$	$21.32^{+0.18}_{-0.20}$	$1.48^{+0.20}_{-0.26}$	$0.514^{+0.027}_{-0.029}$	$3.87^{+0.10}_{-0.11}$	$-0.416^{+0.034}_{-0.034}$	$2.61^{+0.09}_{-0.10}$	$-0.640^{+0.043}_{-0.044}$
Uniform-z	$-1.89^{+0.08}_{-0.10}$	$21.17^{+0.17}_{-0.13}$	$1.50^{+0.19}_{-0.21}$	$0.563^{+0.028}_{-0.025}$	$3.96^{+0.079}_{-0.078}$	$-0.423^{+0.024}_{-0.025}$	$2.26^{+0.13}_{-0.12}$	$-0.690^{+0.058}_{-0.060}$
Single-z	$-1.89^{+0.06}_{-0.07}$	$21.09^{+0.16}_{-0.11}$	$1.32^{+0.21}_{-0.21}$	$0.527^{+0.027}_{-0.026}$	$4.19^{+0.13}_{-0.13}$	$-0.540^{+0.049}_{-0.046}$	$2.55^{+0.08}_{-0.08}$	$-0.546^{+0.029}_{-0.031}$

Table 3. Best-fitting parameters for SF and AGN for the COSMOS and XMM–LSS fields. We fit a PLE model for SF galaxies ($\alpha_L^{\rm SF}$ and $\beta_L^{\rm SF}$) and a PDE model for AGN ($\alpha_D^{\rm AGN}$ and $\beta_D^{\rm AGN}$). The local AGN LF parameters are held fixed in all fits (see Table 2).

Field	$\log(\phi_*^{\rm SF}/{\rm Mpc^{-3}\,dex^{-1}})$	$\log(L_*^{\rm SF}/{\rm W\,Hz^{-1}})$	δ	σ	$\alpha_L^{\rm SF}$	$\beta_L^{\rm SF}$	$\alpha_D^{\rm AGN}$	$\beta_D^{\rm AGN}$
COSMOS	$-1.79^{+0.08}_{-0.15}$	$21.26^{+0.18}_{-0.20}$	$1.55^{+0.33}_{-0.43}$	$0.46^{+0.04}_{-0.04}$	$4.56^{+0.35}_{-0.34}$	$-0.73^{+0.14}_{-0.15}$	$1.41^{+0.27}_{-0.28}$	$-0.40^{+0.11}_{-0.11}$
XMM–LSS	$-2.15^{+0.10}_{-0.13}$	$21.40^{+0.18}_{-0.21}$	$1.49^{+0.19}_{-0.26}$	$0.50^{+0.03}_{-0.03}$	$3.91^{+0.12}_{-0.11}$	$-0.42^{+0.03}_{-0.04}$	$2.79^{+0.10}_{-0.10}$	$-0.67^{+0.04}_{-0.05}$

Fig. B3 shows the SFRD obtained from our uniform-z approach. When compared with our $z > 1$ approach, both methods recover the same overall shape a rise to a broad maximum at $z \sim 2$ followed by a gradual decline and statistically consistent evolution parameters. Refitting the RLF leads to small, compensating shifts in the local SFG parameters, keeping the overall SFRD offset modest. The two confidence envelopes overlap across the full-redshift range, confirming that the SFRD shape and peak position remain unchanged within the combined uncertainties. Fig. B6 shows the SFRD obtained derived using the results of using just the single best-fitting redshift analysis. The two curves (evolving-q and fixed-q) are nearly identical across the full-redshift range, with modest differences. Table 2 shows the best-fitting parameters obtained using the single-redshift approach, consistent with the PDF–based solutions within uncertainties.

5.4 Field-to-field variations

Although we are relatively limited in terms of assessing the level of cosmic variance between the two fields. We can compare the best-fit RLF for each field independently, the results are shown in Table 3 with the RLFs shown in Figs C1 and C2. We find that the fits are formally consistent across all the key parameters, albeit with some interesting small differences. The normalisation for the SFGs in the COSMOS field is a factor of ~ 0.2 dex higher at the knee of the SFG luminosity function. This is coupled with a higher degree of evolution, marginally increasing the difference at $z \sim 0.2$, our lowest redshift bin. This suggests that COSMOS has 60 per cent higher density at ~ 0.2 than the XMM–LSS field. It would be difficult to attribute this to poor photometric redshifts in the XMM–LSS field, given that the performance of the photometric redshift algorithm used in P. W. Hatfield et al. (2022) is most accurate at $0.2 < z < 0.5$, due to the wealth of training data for the GPz algorithm. As such, it is likely due to a genuinely higher comoving space density in the COSMOS field. However, such an 'overdensity' does not necessarily have to be at low redshift. Due to the method of inferring the best-fitting radio luminosity parameters across all redshift bins, then an overdensity at moderately high redshift can also lead to an elevated $\phi_*^{\rm SF}$. Indeed, COSMOS is well known to have a significant overdensity at $z \sim 1$ and this can also be seen in Fig. 1, which in turn can drive up the evolution term. This highlights how just studying a single, relatively narrow field, across a significant redshift range can lead to differing results and conclusions. Importantly, moving forward, we will have both wide and deep radio data coupled with wide and deep optical data over the full MIGHTEE fields to address this issue fully.

6 SUMMARY AND CONCLUSIONS

We have measured the evolution of the RLF for SFGs and AGN using deep 1.28 GHz MeerKAT observations from the MIGHTEE survey, combining the COSMOS and XMM–LSS fields. The total RLF was decomposed into SFG and AGN components and modelled with PLE for SFGs and PDE for AGN.

We adopt a new approach to account for photometric redshift uncertainties and incompleteness due to some radio sources not having an optical identification and therefore redshift. Spectroscopic redshifts are adopted where available and, for sources without spectroscopy, we propagate full photometric redshift PDFs through 100 Monte-Carlo resamples to generate robust uncertainties on $V_{\rm max}$ and the binned LFs. This Monte-Carlo PDF propagation both broadens the uncertainties to include redshift error and reduces Poisson-driven spikes at the bright-end of the RLF by redistributing redshift probability across bins.

To assess sensitivity to optical/NIR identification incompleteness, we employ three different approaches. Our primary analysis assigns all non-identified sources to $z > 1$, providing a clear upper bound on their high-z impact. As alternative cross-checks, we distribute the same sources uniformly in z and also adopt a single–redshift analysis that assigns one best redshift per source and then

redetermine the RLF. All three analyses produce consistent RLFs within the combined uncertainties; differences are confined to modest, localized shifts.

We find a much higher normalisation for the SFG luminosity function compared to previous studies at 3 GHz over the COSMOS field by M. Novak et al. (2017), however, our results are consistent with more recent studies with both MeerKAT (A. M. Matthews et al. 2024) and LOFAR (R. K. Cochrane et al. 2023). We attribute this to the much better surface brightness sensitivity of the MeerKAT (and LOFAR) telescopes, compared to the A + C configuration used for the VLA-3GHz COSMOS survey of V. Smolčić et al. (2017a). However, even with this higher normalisation, coupled with a steeper faint-end slope, we still find evidence for strong evolution for the SFG population to $z \sim 2$.

From the radio luminosity function, we infer the evolution in the cosmic SFRD. We determine the SFRD using two radio–SFR calibrations: one where we adopt a fixed linear relationship between radio luminosity and SFR from E. J. Murphy (2009) and one that evolves from this $z = 0$ calibration, with redshift following the work of J. Delhaize et al. (2017) and M. Novak et al. (2017).

Both calibrations show an increase in the SFRDs that exceed the SFRD from UV + IR compilations and also the radio-based work of M. Novak et al. (2017), but are consistent with the A. M. Matthews et al. (2024) radio-based measurements. However, we find that adopting more recent determinations of the correlation between radio luminosity and SFRs from R. H. W. Cook et al. (2024), based on full spectral energy distribution modelling of the MIGHTEE continuum data, can reconcile the SFRD with UV and infrared tracers of the SFRD.

Given the interplay between the calibration of the radio luminosity–SFR calibration and the SFRD through the luminosity function, it is critical to adopt consistent calibrations and assumptions when combining these. Indeed, if there is also a mass-dependent aspect to the relationship between the SFR and radio luminosity, then this also needs to be included as a factor in the determination of the SFRD based on radio continuum data.

However, if the radio continuum emission can be properly calibrated against robust measurements of the SFR across all stellar masses, overcoming the various Malmquist bias effects, then it is clear that the new generation of radio telescopes are a tremendously powerful probe of the evolution in the total, both obscured and unobscured, SFRD. Moreover, E. D. Malefahlo et al. (2026) have recently shown that utilizing new Bayesian source extraction methods based on the multiwavelength catalogues, enables robust flux-density measurement much closer to the confusion noise, opening up the potential to determine the RLF to significantly fainter flux-densities. Thus, the full MIGHTEE radio continuum data when fully cross-matched with both current and forthcoming data from Rubin and *Euclid*, should provide the most robust measurement of the evolution in both the SFRD, where depth is critical, and the evolution of the radio-AGN activity, where areal coverage becomes increasingly important.

Furthermore, this study shows that these different components can be modelled separately in a combined radio luminosity function, thus mitigating against issues surrounding classifying sources as AGN or star-formation-dominated galaxies. Indeed, the statistical measurement of both populations may provide more robust and unbiased insights, as it naturally accounts for hybrid sources.

ACKNOWLEDGEMENTS

We thank the anonymous referee for their useful comments that helped to improve this paper. MJJ, CLH, and IHW acknowledge support from the Hintze Family Charitable Foundation through the Oxford Hintze Centre for Astrophysical Surveys. MJJ, IH, RGV, and NS acknowledge the support from a UKRI Frontiers Research Grant [EP/X026639/1]. CLH also acknowledges support from the Science and Technology Facilities Council (STFC) through grant ST/Y000951/1. CP acknowledges support via the RAL Space In House Research programme funded by the Science and Technology Facilities Council of the UK Research and Innovation (award ST/M001083/1). MV acknowledges financial support from the Inter-University Institute for Data Intensive Astronomy (IDIA), a partnership of the University of Cape Town, the University of Pretoria and the University of the Western Cape, and from the South African Department of Science and Innovation's National Research Foundation under the ISARP RADIOMAP Joint Research Scheme (DSI-NRF Grant Number 150551) and the CPRR HIPPO Project (DSI-NRF Grant Number SRUG22031677).

The MeerKAT telescope is operated by the South African Radio Astronomy Observatory, which is a facility of the National Research Foundation, an agency of the Department of Science and Innovation. We acknowledge the use of the ilifu cloud computing facility – www.ilifu.ac.za, a partnership between the University of Cape Town, the University of the Western Cape, Stellenbosch University, Sol Plaatje University and the Cape Peninsula University of Technology. The Ilifu facility is supported by contributions from the Inter-University Institute for Data Intensive Astronomy (IDIA – a partnership between the University of Cape Town, the University of Pretoria and the University of the Western Cape, the Computational Biology division at UCT and the Data Intensive Research Initiative of South Africa (DIRISA). The authors acknowledge the Centre for High Performance Computing (CHPC), South Africa, for providing computational resources to this research project.

DATA AVAILABILITY

The MIGHTEE ES data products are available from the SARAO archive at https://doi.org/10.48479/emmd-kf31.

REFERENCES

Adams N. J., Bowler R. A. A., Jarvis M. J., Varadaraj R. G., Häußler B., 2023, MNRAS, 523, 327
Aihara H. et al., 2018a, PASJ, 70, S4
Aihara H. et al., 2018b, PASJ, 70, S8
Aihara H. et al., 2019, PASJ, 71, 114
Algera H. S. B. et al., 2020, ApJ, 903, 138
Almosallam I. A., Lindsay S. N., Jarvis M. J., Roberts S. J., 2016a, MNRAS, 455, 2387
Almosallam I. A., Jarvis M. J., Roberts S. J., 2016b, MNRAS, 462, 726
Arnaudova M. I. et al., 2025, MNRAS, 542, 2245
Arnouts S. et al., 2005, ApJ, 619, L43
Bell E. F., 2003, ApJ, 586, 794
Best P. N., Heckman T. M., 2012, MNRAS, 421, 1569
Bowler R. A. A., Adams N. J., Jarvis M. J., Häußler B., 2021, MNRAS, 502, 662
Buchner J. et al., 2014, A&A, 564, A125
Cattaneo A. et al., 2009, Nature, 460, 213
Clewley L., Jarvis M. J., 2004, MNRAS, 352, 909
Cochrane R. K. et al., 2023, MNRAS, 523, 6082

Condon J. J., 1992a, ARA&A, 30, 575
Condon J. J., 1992b, ARA&A, 30, 575
Condon J. J., Kellermann K. I., Kimball A. E., Ivezić Ž., Perley R. A., 2013, ApJ, 768, 37
Cook R. H. W. et al., 2024, MNRAS, 531, 708
Cuillandre J.-C. J. et al., 2012, in Peck A. B., Seaman R. L., Comeron F., eds, Proc. SPIE Conf. Ser. Vol. 8448, Observatory Operations: Strategies, Processes, and Systems IV. SPIE , Bellingham, p. 84480M
DESI Collaboration, 2024, AJ, 168, 58
Davé R., Anglés-Alcázar D., Narayanan D., Li Q., Rafieferantsoa M. H., Appleby S., 2019, MNRAS, 486, 2827
Davies L. J. M. et al., 2017, MNRAS, 466, 2312
Delhaize J. et al., 2017, A&A, 602, A4
Delhaize J. et al., 2021, MNRAS, 501, 3833
Delvecchio I. et al., 2021, A&A, 647, A123
Duncan K. J., Jarvis M. J., Brown M. J. I., Röttgering H. J. A., 2018, MNRAS, 477, 5177
Duncan K. J. et al., 2021, A&A, 648, A4
Dunlop J. S., Peacock J. A., 1990, MNRAS, 247, 19
Enia A. et al., 2022, ApJ, 927, 204
Fabian A. C., 2012, ARA&A, 50, 455
Feroz F., Hobson M. P., 2008, MNRAS, 384, 449
Gentile F. et al., 2024, ApJ, 962, 26
Gentile F. et al., 2025, A&A, 697, A46
Gürkan G. et al., 2018, MNRAS, 475, 3010
Hale C. L., Jarvis M. J., Delvecchio I., Hatfield P. W., Novak M., Smolčić V., Zamorani G., 2018, MNRAS, 474, 4133
Hale C. L. et al., 2023, MNRAS, 520, 2668
Hamlett J. et al., 2026, MNRAS, 547, 468
Hardcastle M. J., Croston J. H., 2020, New A Rev., 88, 101539
Hatfield P. W., Jarvis M. J., Adams N., Bowler R. A. A., Häußler B., Duncan K. J., 2022, MNRAS, 513, 3719
Heckman T. M., Best P. N., 2014, ARA&A, 52, 589
Heckman T. M., Roy N., Best P. N., Kondapally R., 2024, ApJ, 977, 125
Helou G., Soifer B. T., Rowan-Robinson M., 1985, ApJ, 298, L7
Heywood I. et al., 2022, MNRAS, 509, 2150
Ilbert O. et al., 2009, ApJ, 690, 1236
Jarvis M. et al., 2016, in MeerKAT Science: On the Pathway to the SKA. PoS(MeerKAT2016)006, SISSA, Trieste, p. 6
Jarvis M. J., Rawlings S., Willott C. J., Blundell K. M., Eales S., Lacy M., 2001, MNRAS, 327, 907
Jarvis M. J. et al., 2010, MNRAS, 409, 92
Jarvis M. J. et al., 2013, MNRAS, 428, 1281
Karim A. et al., 2011, ApJ, 730, 61
Kennicutt R. C. Jr, 1998, ARA&A, 36, 189
Kennicutt R. C., Evans N. J., 2012, ARA&A, 50, 531
Khostovan A. A. et al., 2026, ApJS, 282, 6
Kimball A. E., Kellermann K. I., Condon J. J., Ivezić Ž., Perley R. A., 2011, ApJ, 739, L29
Kondapally R. et al., 2022, MNRAS, 513, 3742
Kondapally R. et al., 2023, MNRAS, 523, 5292
Koprowski M. P., Dunlop J. S., Michałowski M. J., Coppin K. E. K., Geach J. E., McLure R. J., Scott D., van der Werf P. P., 2017, MNRAS, 471, 4155
Lindsay S. N. et al., 2014, MNRAS, 440, 1527
Macfarlane C. et al., 2021, MNRAS, 506, 5888
Madau P., Dickinson M., 2014, ARA&A, 52, 415
Magliocchetti M., Popesso P., Brusa M., Salvato M., Laigle C., McCracken H. J., Ilbert O., 2017, MNRAS, 464, 3271
Malefahlo E., Santos M. G., Jarvis M. J., White S. V., Zwart J. T. L., 2020, MNRAS, 492, 5297
Malefahlo E. D., Jarvis M. J., Santos M. G., White S. V., Adams N. J., Bowler R. A. A., 2022, MNRAS, 509, 4291
Malefahlo E. D. et al., 2026, MNRAS, 547, stag285
Marshall H. L., 1985, ApJ, 299, 109
Matthews A. M., Condon J. J., Cotton W. D., Mauch T., 2021, ApJ, 914, 126
Matthews A. M. et al., 2024, ApJ, 966, 194
Mauch T., Sadler E. M., 2007, MNRAS, 375, 931
McAlpine K., Jarvis M. J., 2011, MNRAS, 413, 1054
McAlpine K., Jarvis M. J., Bonfield D. G., 2013, MNRAS, 436, 1084
McCracken H. J. et al., 2012, A&A, 544, A156
Mohan N., Rafferty D., 2015, Astrophysics Source Code Library, record ascl:1502.007
Morabito L. K. et al., 2025, MNRAS, 536, L32
Moster B. P., Somerville R. S., Newman J. A., Rix H.-W., 2011, ApJ, 731, 113
Murphy E. J., 2009, ApJ, 706, 482
Murphy E. J. et al., 2011, ApJ, 737, 67
Muxlow T. W. B. et al., 2020, MNRAS, 495, 1188
Novak M. et al., 2017, A&A, 602, A5
Novak M., Smolčić V., Schinnerer E., Zamorani G., Delvecchio I., Bondi M., Delhaize J., 2018, A&A, 614, A47
Oke J. B., Gunn J. E., 1983, ApJ, 266, 713
Petter G. C., Hickox R. C., Morabito L. K., Alexander D. M., 2024, ApJ, 972, 184
Pracy M. B. et al., 2016, MNRAS, 460, 2
Radcliffe J. F., Barthel P. D., Thomson A. P., Garrett M. A., Beswick R. J., Muxlow T. W. B., 2021, A&A, 649, A27
Read S. C. et al., 2018, MNRAS, 480, 5625
Rigby E. E., Best P. N., Brookes M. H., Peacock J. A., Dunlop J. S., Röttgering H. J. A., Wall J. V., Ker L., 2011, MNRAS, 416, 1900
Sabater J. et al., 2021, A&A, 648, A2
Saunders W., Rowan-Robinson M., Lawrence A., Efstathiou G., Kaiser N., Ellis R. S., Frenk C. S., 1990, MNRAS, 242, 318
Schmidt M., 1968, ApJ, 151, 393
Smith D. J. B. et al., 2021a, A&A, 648, A6
Smith D. J. B. et al., 2021b, A&A, 648, A6
Smolčić V. et al., 2009, ApJ, 696, 24
Smolčić V. et al., 2017a, A&A, 602, A1
Smolčić V. et al., 2017b, A&A, 602, A6
Tabatabaei F. et al., 2025, ApJ, 989, 44
Tasse C. et al., 2021, A&A, 648, A1
Vaccari M., 2022, in Zenodo dataset. Geneva (CERN), Zenodo, p. 6368348
Varadaraj R. G., Bowler R. A. A., Jarvis M. J., Adams N. J., Häußler B., 2023, MNRAS, 524, 4586
Varadaraj R. G. et al., 2026, MNRAS, A239
Wang L. et al., 2019, A&A, 631, A109
White S. V., Jarvis M. J., Häußler B., Maddox N., 2015, MNRAS, 448, 2665
White S. V., Jarvis M. J., Kalfountzou E., Hardcastle M. J., Verma A., Cao Orjales J. M., Stevens J., 2017, MNRAS, 468, 217
Whittam I. H. et al., 2024, MNRAS, 527, 3231
Whittam I. H. et al., 2025, MNRAS, 543, 507
Willott C. J., Rawlings S., Blundell K. M., Lacy M., Eales S. A., 2001, MNRAS, 322, 536
Wilman R. J. et al., 2008, MNRAS, 388, 1335
Yue B. H. et al., 2025, MNRAS, 537, 858
Yun M. S., Reddy N. A., Condon J. J., 2001, ApJ, 554, 803
Zhu S., Brandt W. N., Zou F., Luo B., Ni Q., Xue Y., Yan W., 2023, MNRAS, 522, 3506

APPENDIX A: SOURCE COUNTS AND LUMINOSITY FUNCTION

Table A1. Summary of the redshift-bin source counts (spectroscopic, photometric, and non-XID) used in the $V_{\rm max}$ calculation for the luminosity function analysis.

Table A1. Luminosity functions of the total radio-selected sample obtained with the V_{max} method for the $z > 1$ analysis. Source counts per redshift bin for the COSMOS and XMM–LSS fields, including spectroscopic redshifts (N_{spec}), photometric redshifts (N_{phot}, counted only when N_{spec} is not available), and sources without optical counterparts (N_{noXID}), assigned statistical redshifts at $z > 1$.

Redshift	$\log(L_{1.4GHz}/W\,Hz^{-1})$	$\log(\phi/Mpc^{-3}\,dex^{-1})$	COSMOS N_{spec}	COSMOS N_{phot}	COSMOS N_{noXID}	XMM N_{spec}	XMM N_{phot}	XMM N_{noXID}
$0.2 < z < 0.4$	21.88	-2.15 ± 0.02	71	1	0	116	116	0
	22.12	-2.34 ± 0.02	159	1	0	195	212	0
	22.38	-2.73 ± 0.02	152	1	0	179	168	0
	22.62	-3.14 ± 0.03	86	1	0	86	89	0
	22.88	-3.45 ± 0.04	32	1	0	37	45	0
	23.12	-3.91 ± 0.07	12	1	0	13	17	0
	23.38	-4.10 ± 0.08	8	1	0	13	6	0
	23.62	-4.73 ± 0.18	1	0	0	2	3	0
	23.88	-4.55 ± 0.14	1	0	0	7	1	0
	24.12	-4.90 ± 0.22	1	0	0	2	1	0
	24.38	-4.81 ± 0.18	2	0	0	3	1	0
	24.62	-4.46 ± 0.13	0	0	0	10	1	0
	24.88	-5.52 ± 0.43	0	0	0	0	1	0
	25.12	-5.52 ± 0.43	0	0	0	0	1	0
	25.38	-5.52 ± 0.43	0	0	0	0	1	0
$0.4 < z < 0.6$	22.62	-2.60 ± 0.05	135	5	0	324	394	0
	22.88	-3.15 ± 0.02	95	3	0	195	223	0
	23.12	-3.62 ± 0.03	34	3	0	61	78	0
	23.38	-3.93 ± 0.05	10	1	0	36	39	0
	23.62	-4.43 ± 0.08	2	1	0	12	13	0
	23.88	-4.70 ± 0.11	3	1	0	8	3	0
	24.12	-5.00 ± 0.16	0	1	0	5	2	0
	24.38	-5.06 ± 0.18	1	1	0	3	2	0
	24.62	-5.54 ± 0.31	0	0	0	2	1	0
	24.88	-5.25 ± 0.22	1	0	0	3	1	0
	25.12	-5.85 ± 0.43	0	0	0	0	1	0
	25.38	-5.86 ± 0.43	0	0	0	0	1	0
	25.62	-5.86 ± 0.43	0	0	0	0	1	0
	25.88	-5.86 ± 0.43	0	0	0	0	1	0
$0.6 < z < 0.8$	23.12	-3.21 ± 0.02	115	9	0	241	282	0
	23.38	-3.60 ± 0.02	60	7	0	109	117	0
	23.62	-4.00 ± 0.04	33	2	0	39	42	0
	23.88	-4.35 ± 0.05	9	1	0	21	21	0
	24.12	-4.65 ± 0.07	9	1	0	7	11	0
	24.38	-4.81 ± 0.10	5	1	0	7	5	0
	24.62	-4.69 ± 0.09	1	1	0	15	6	0
	24.88	-5.19 ± 0.18	0	1	0	5	2	0
	25.12	-5.17 ± 0.12	0	0	0	7	1	0
	25.38	-5.57 ± 0.19	0	0	0	2	1	0
	25.62	-6.05 ± 0.31	0	0	0	1	1	0
	25.88	-6.05 ± 0.69	0	0	0	0	1	0
	26.20	-5.35 ± 0.40	0	0	0	8	1	0
$0.8 < z < 1.0$	23.38	-3.26 ± 0.02	143	18	0	198	442	0
	23.62	-3.65 ± 0.02	59	12	0	81	190	0
	23.88	-4.02 ± 0.04	18	4	0	39	79	0
	24.12	-4.35 ± 0.05	13	1	0	22	33	0
	24.38	-4.62 ± 0.07	9	2	0	11	14	0
	24.62	-4.86 ± 0.10	4	1	0	7	9	0
	24.88	-4.79 ± 0.09	3	1	0	13	6	0
	25.12	-5.38 ± 0.18	2	0	0	2	2	0
	25.38	-5.05 ± 0.12	3	0	0	6	4	0
	25.62	-5.46 ± 0.19	0	0	0	3	2	0

Table A1 – *continued*

Redshift	$\log(L_{1.4\mathrm{GHz}}/\mathrm{W\,Hz^{-1}})$	$\log(\phi/\mathrm{Mpc^{-3}\,dex^{-1}})$	COSMOS N_{spec}	COSMOS N_{phot}	COSMOS N_{noXID}	XMM N_{spec}	XMM N_{phot}	XMM N_{noXID}
	25.88	-5.87 ± 0.31	0	0	0	0	2	0
	26.20	-6.38 ± 0.69	0	0	0	0	1	0
	26.60	-5.90 ± 0.40	0	0	0	3	1	0
$1.0 < z < 1.3$	23.62	-3.69 ± 0.02	86	14	61	82	367	46
	23.88	-4.06 ± 0.03	39	8	45	48	158	29
	24.12	-4.43 ± 0.04	21	3	19	19	64	38
	24.38	-4.73 ± 0.06	9	3	6	13	30	23
	24.62	-5.18 ± 0.10	0	1	3	6	12	27
	24.88	-5.28 ± 0.12	1	2	1	4	7	6
	25.12	-5.22 ± 0.11	7	1	0	6	3	2
	25.38	-5.42 ± 0.14	0	0	0	4	7	1
	25.62	-5.58 ± 0.16	0	0	0	1	6	2
	25.88	-6.42 ± 0.43	0	0	0	0	1	2
	26.20	-6.64 ± 0.69	0	0	0	0	1	0
	26.60	-6.64 ± 0.69	0	0	0	0	1	0
$1.3 < z < 1.6$	23.88	-3.86 ± 0.01	55	17	69	35	340	29
	24.12	-4.20 ± 0.02	26	7	26	17	147	45
	24.38	-4.62 ± 0.04	12	2	4	6	58	24
	24.62	-5.02 ± 0.06	4	1	6	0	26	27
	24.88	-5.20 ± 0.10	2	1	1	1	17	21
	25.12	-5.31 ± 0.11	1	1	0	2	12	5
	25.38	-5.64 ± 0.15	0	1	1	0	6	3
	25.62	-5.79 ± 0.15	0	0	0	0	5	4
	25.88	-5.80 ± 0.25	0	0	0	0	5	2
	26.20	-5.79 ± 0.49	0	0	0	5	3	2
	26.60	-6.71 ± 0.69	1	0	0	0	1	0
	27.00	-6.71 ± 0.69	0	0	0	0	1	0
$1.6 < z < 2.0$	23.88	-3.50 ± 0.02	29	17	51	27	589	31
	24.12	-4.09 ± 0.02	27	19	34	17	338	44
	24.38	-4.41 ± 0.03	17	5	18	9	137	52
	24.62	-4.80 ± 0.05	3	3	9	6	53	40
	24.88	-5.21 ± 0.08	1	1	1	1	20	29
	25.12	-5.27 ± 0.09	0	1	0	5	12	18
	25.38	-5.40 ± 0.10	0	2	0	1	6	5
	25.62	-5.65 ± 0.14	0	1	0	1	7	3
	25.88	-5.95 ± 0.19	0	0	0	0	3	2
	26.20	-6.02 ± 0.26	0	0	0	0	2	1
	26.60	-6.87 ± 0.69	0	0	0	0	1	3
	27.00	-6.87 ± 0.69	0	0	0	0	1	0
	27.40	-6.87 ± 0.69	0	0	0	1	0	0
$2.0 < z < 2.5$	24.12	-3.96 ± 0.02	37	16	23	12	314	19
	24.38	-4.45 ± 0.03	18	11	21	12	158	31
	24.62	-4.77 ± 0.04	7	3	12	7	65	19
	24.88	-5.10 ± 0.06	5	1	1	2	25	16
	25.12	-5.27 ± 0.08	1	1	0	3	10	19
	25.38	-5.46 ± 0.09	0	1	1	0	7	16
	25.62	-5.51 ± 0.10	2	1	0	3	4	9
	25.88	-5.72 ± 0.13	0	1	0	1	3	7
	26.20	-5.86 ± 0.19	3	0	1	0	2	8
	26.60	-6.69 ± 0.49	0	0	0	1	1	1
	27.00	-6.69 ± 0.49	0	0	0	0	1	2
	27.40	-6.69 ± 0.49	0	0	0	0	2	0
$2.5 < z < 3.3$	24.38	-4.24 ± 0.03	20	11	33	9	251	13
	24.62	-4.79 ± 0.03	18	5	16	5	113	14

Table A1 – *continued*

Redshift	$\log(L_{1.4\mathrm{GHz}}/\mathrm{W\,Hz^{-1}})$	$\log(\phi/\mathrm{Mpc^{-3}\,dex^{-1}})$	COSMOS N_{spec}	COSMOS N_{phot}	COSMOS N_{noXID}	XMM N_{spec}	XMM N_{phot}	XMM N_{noXID}
	24.88	-5.11 ± 0.05	2	4	7	1	47	15
	25.12	-5.34 ± 0.06	5	1	1	1	17	22
	25.38	-5.52 ± 0.08	2	1	1	0	8	11
	25.62	-5.78 ± 0.11	1	1	2	0	8	11
	25.88	-6.19 ± 0.18	0	1	0	0	3	19
	26.20	-6.17 ± 0.22	1	0	0	0	2	18
	26.60	-6.48 ± 0.31	0	0	0	0	2	6
	27.00	-7.19 ± 0.69	0	0	0	0	1	1
	27.40	-7.19 ± 0.69	0	0	0	0	1	0
	27.80	-7.19 ± 0.43	0	0	0	0	0	1
	28.20	-7.19 ± 0.43	0	0	0	0	0	1
$3.3 < z < 4.6$	24.62	-4.90 ± 0.43	4	2	9	4	67	4
	24.88	-5.62 ± 0.43	6	2	1	1	26	0
	25.12	-5.93 ± 0.43	3	1	4	0	10	3
	25.38	-6.17 ± 0.43	2	1	1	0	5	3
	25.62	-6.69 ± 0.43	1	1	0	0	1	1
	25.88	-6.01 ± 0.43	0	1	0	0	1	13
	26.20	-5.77 ± 0.43	0	0	1	0	1	36
	26.60	-5.90 ± 0.43	0	0	0	0	1	27
	27.00	-6.35 ± 0.43	0	0	0	0	1	9
	27.40	-6.88 ± 0.43	0	0	0	0	1	3
	27.80	-7.36 ± 0.43	0	0	0	0	0	1

APPENDIX B: ALTERNATIVE REDSHIFT ASSIGNMENT TESTS

This appendix examines how different redshift assignment methods affect the derived RLFs and SFRDs. In addition to our primary PDF-based analysis with $z > 1$, we test two alternative approaches: a uniform-z assignment for non-XID sources and a single best-z approach. These comparisons allow us to assess the robustness of our evolutionary fits and quantify systematic uncertainties arising from redshift incompleteness. The resulting luminosity functions and SFRD evolution for these tests are shown in Figs B1–B6.

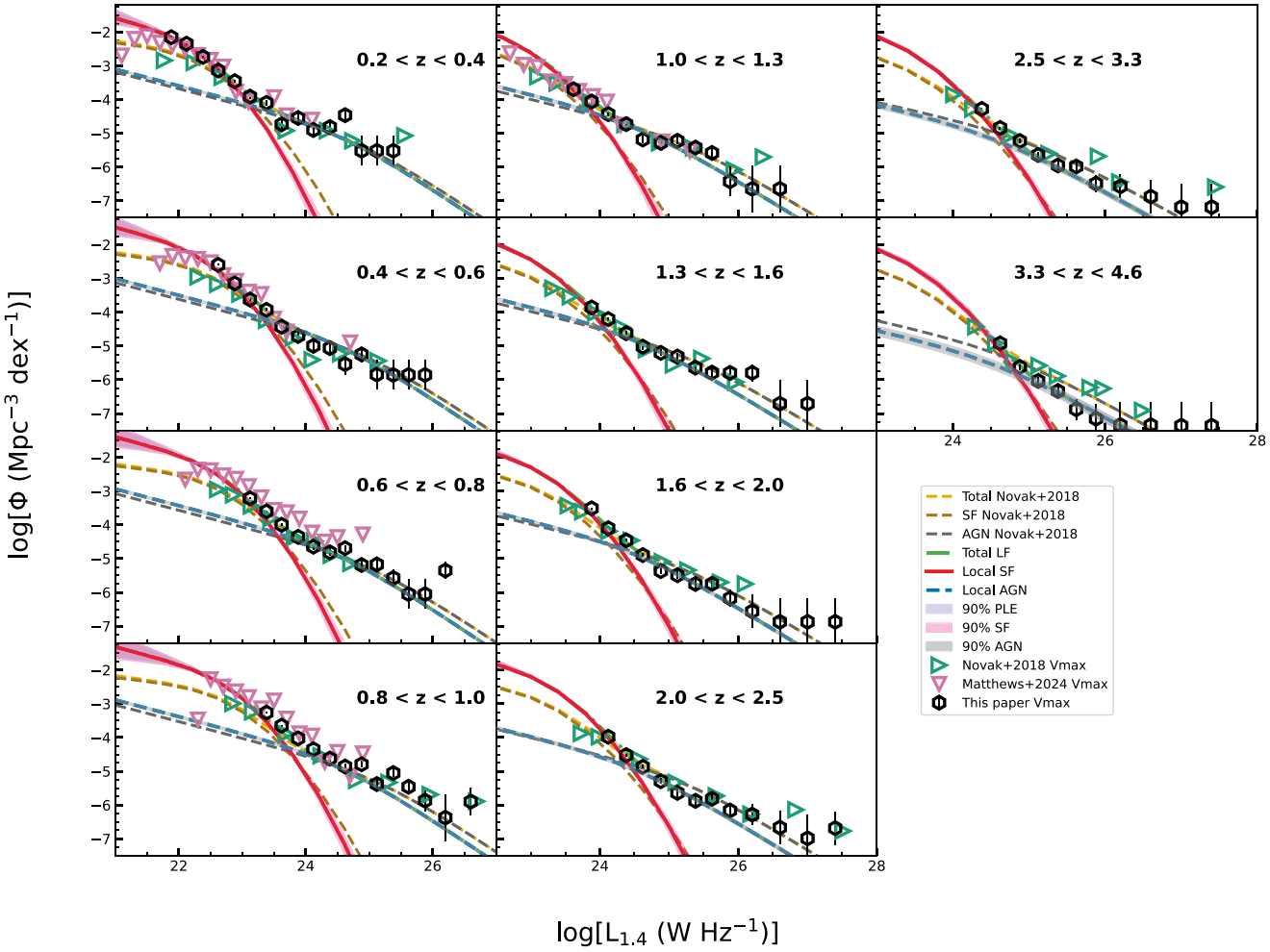

Figure B1. Total 1.4 GHz radio luminosity function (LF) in ten redshift bins when redshifts of non-XID sources are assigned uniformly in z. Black hexagons: $1/V_{\rm max}$ measurements from this work, including statistical redshifts for radio sources without optical/NIR counterparts. Red solid and blue dashed curves: best-fitting SF (PLE) and AGN (PDE) components; magenta and light-blue bands show their 90 per cent credible intervals. Yellow/brown/grey dashed curves: total, SF, and AGN LFs from M. Novak et al. (2018) for comparison. For reference, $V_{\rm max}$ points from M. Novak et al. (2018) and A. M. Matthews et al. (2024) are also shown as green right-pointing and magenta down-pointing triangles, respectively.

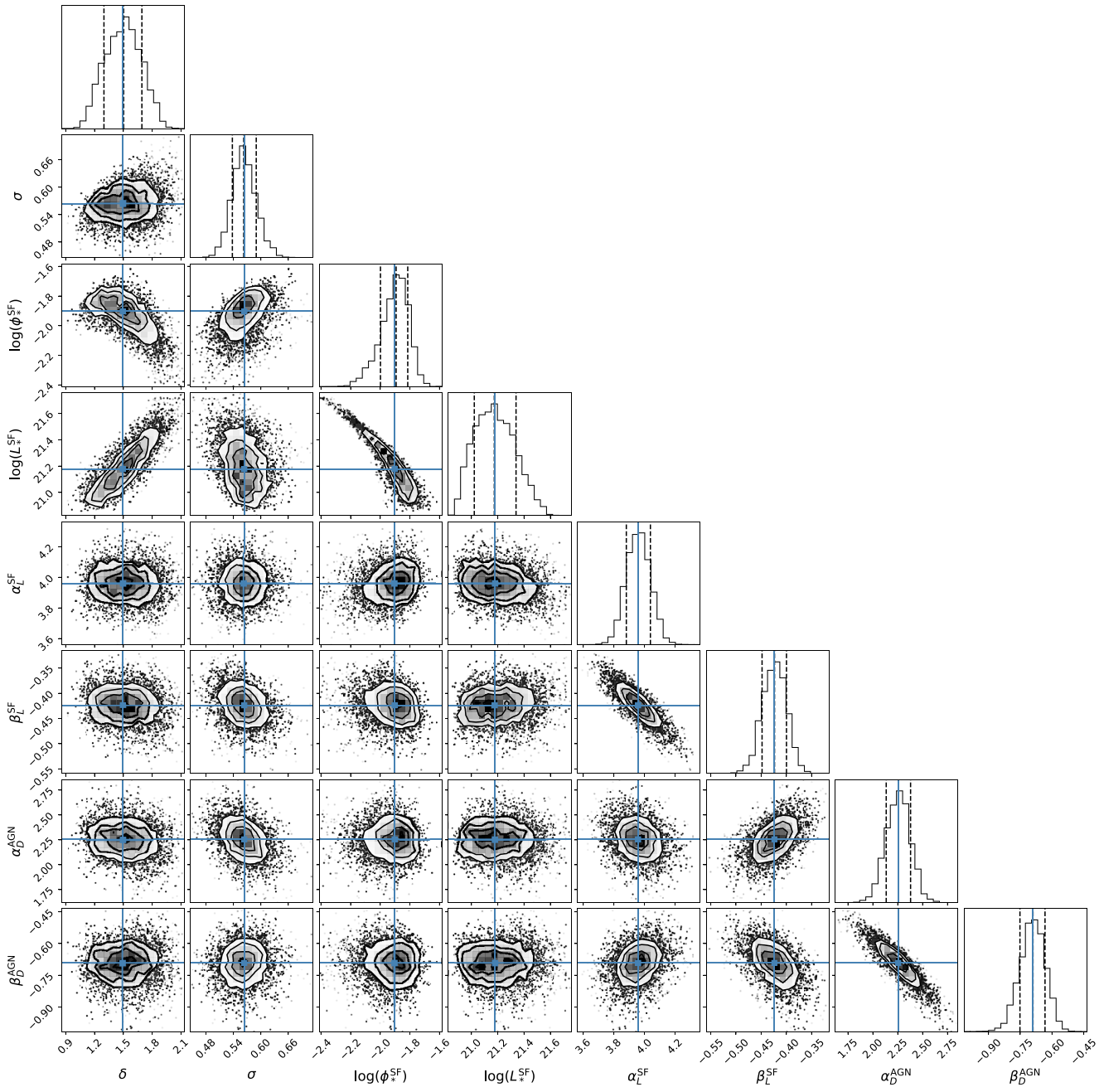

Figure B2. Corner plot displaying the posterior distributions of the eight best-fitting parameters for the total radio LF evolution in the uniform-z analysis.

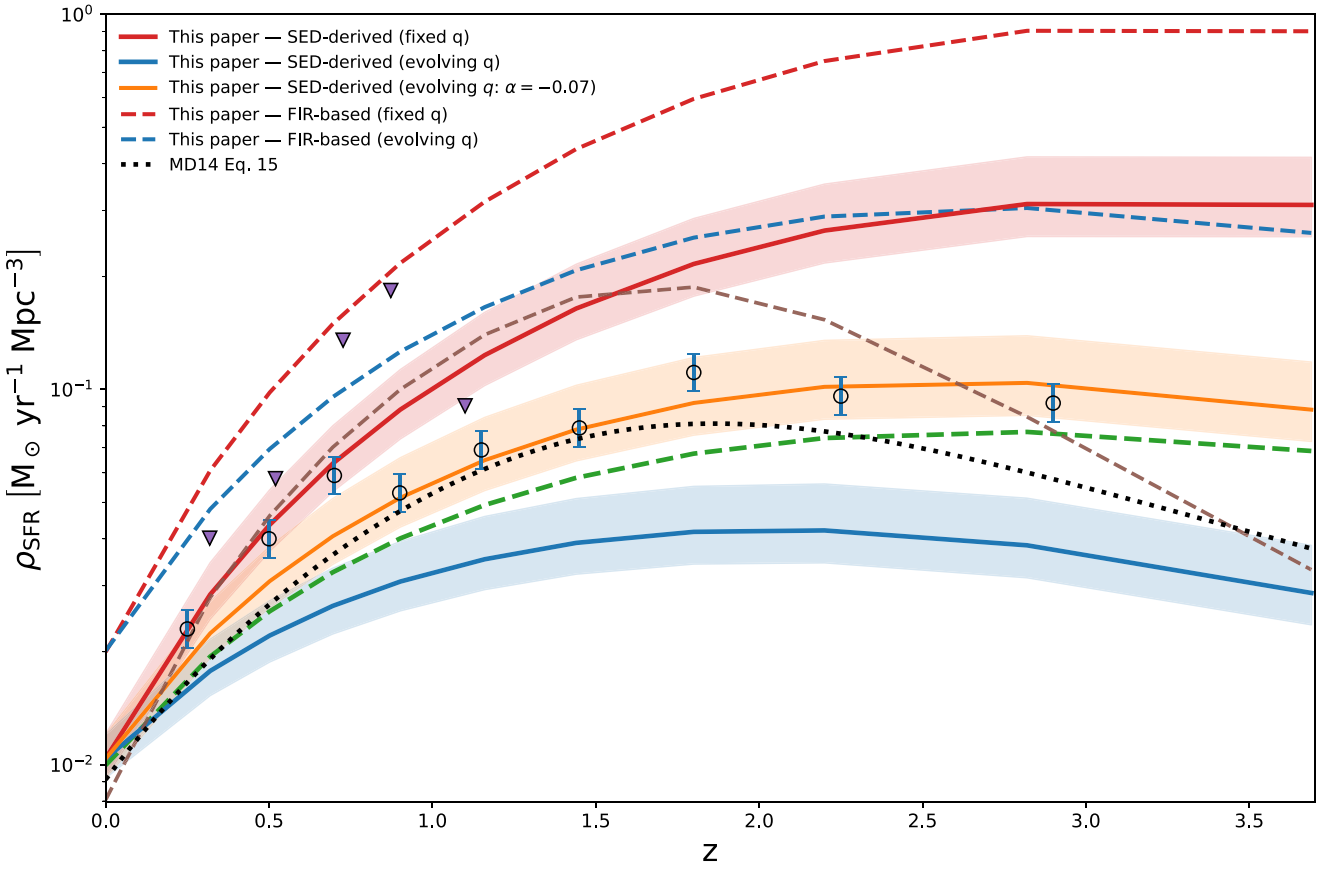

Figure B3. SFRD, $\rho_{\rm SFR}$, as a function of redshift where non-XID radio sources are assigned uniformly in z. Solid lines show the evolution assuming the SED-derived conversion to SFR from radio luminosity (R. H. W. Cook et al. 2024). The fixed-q track is denoted by the red curve (with 68 per cent confidence band) and the evolving-q track by the blue line (with 68 per cent confidence band). We also show an alternative line with $q_{\rm tot} \propto (1+z)^{-0.07}$ (orange). For comparison, the dashed lines show the SFRD based on the FIR-based conversion from radio luminosity to SFR with fixed-q (red) and evolving-q (blue). The brown dashed curve shows the radio-only model from A. M. Matthews et al. (2021). We also show data points from radio-derived SFRD measurements from various literature: M. Novak et al. (2017) (green dashed line), R. K. Cochrane et al. (2023) (open circles with blue error bars) and A. M. Matthews et al. (2024) (purple inverted triangles). The black dotted line is the UV + IR compilation fit of P. Madau & M. Dickinson (2014). We only show the confidence region for our baseline model for clarity.

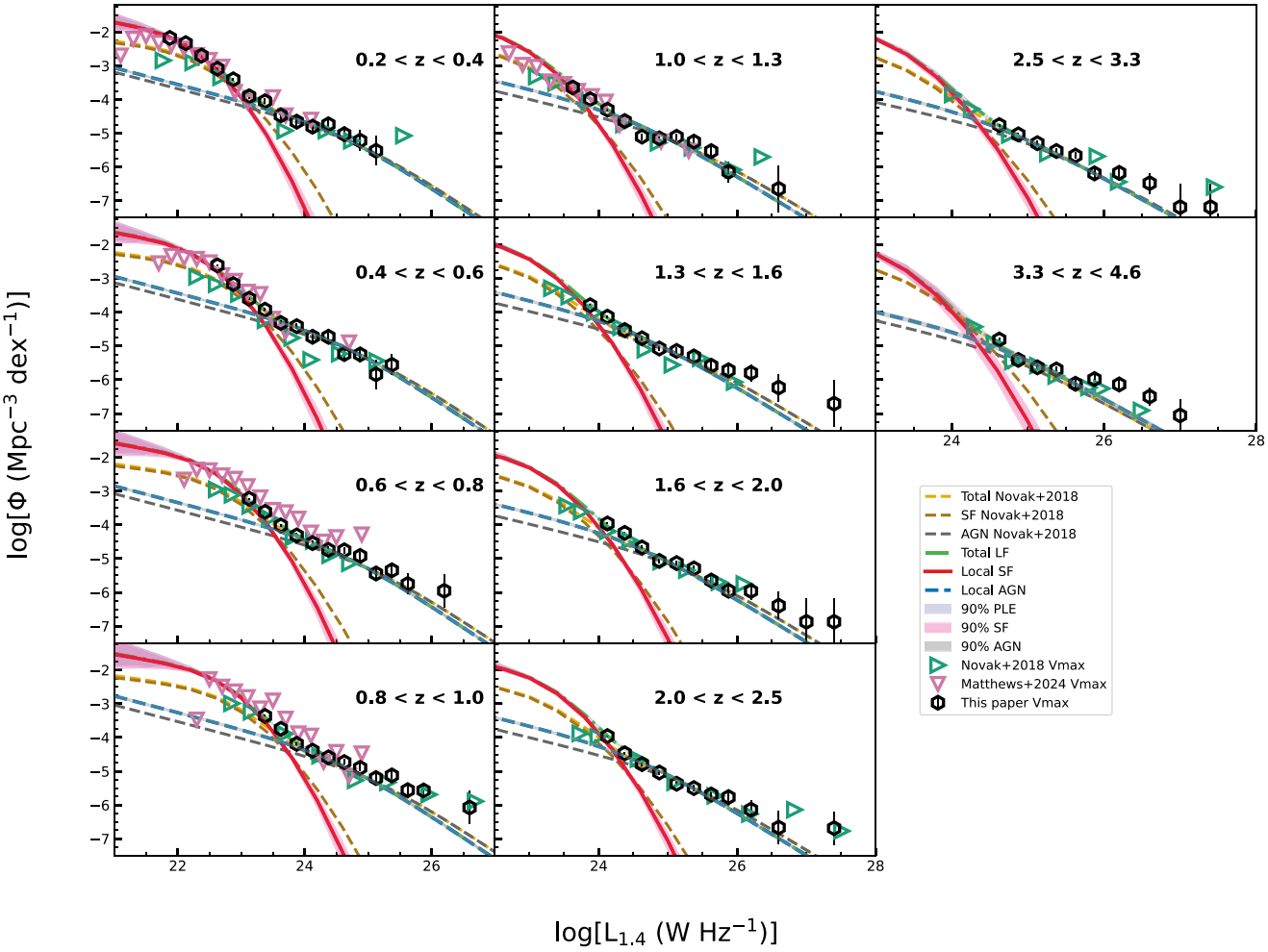

Figure B4. Total 1.4 GHz radio luminosity function (LF) in ten redshift bins from the single-redshift analysis. Black hexagons: $1/V_{\rm max}$ measurements from this work, including statistical redshifts for radio sources without optical/NIR counterparts at $z > 1$. Red solid and blue dashed curves: best-fitting SF (PLE) and AGN (PDE) components; magenta and light-blue bands show their 90 per cent credible intervals. Yellow/brown/grey dashed curves: total, SF, and AGN LFs from M. Novak et al. (2018) for comparison. For reference, $V_{\rm max}$ points from M. Novak et al. (2018) and A. M. Matthews et al. (2024) are also shown as green right-pointing and magenta down-pointing triangles, respectively.

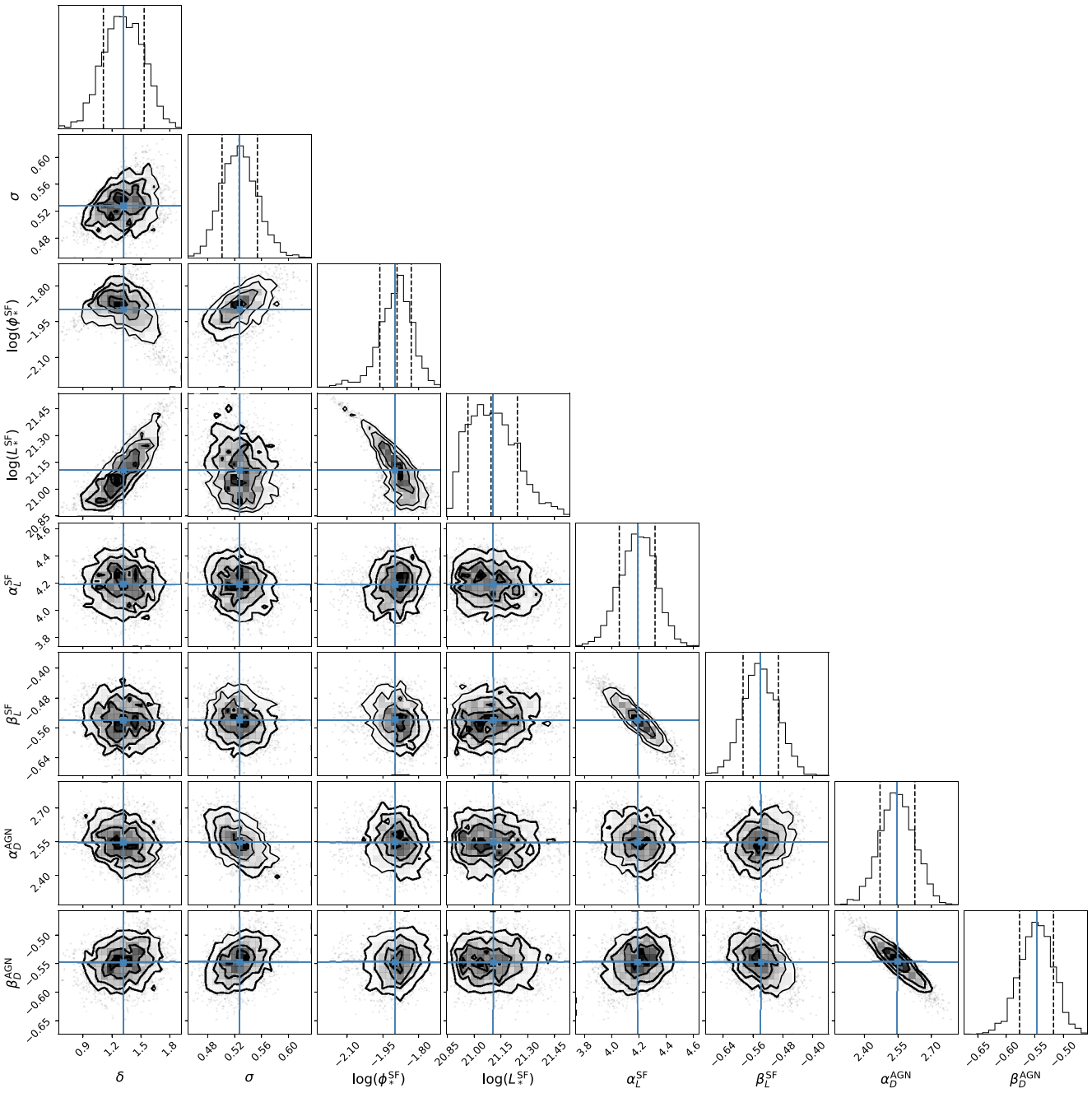

Figure B5. Corner plot displaying the posterior distributions of the eight best-fitting parameters used to describe the total radio LF evolution in the single-redshift analysis.

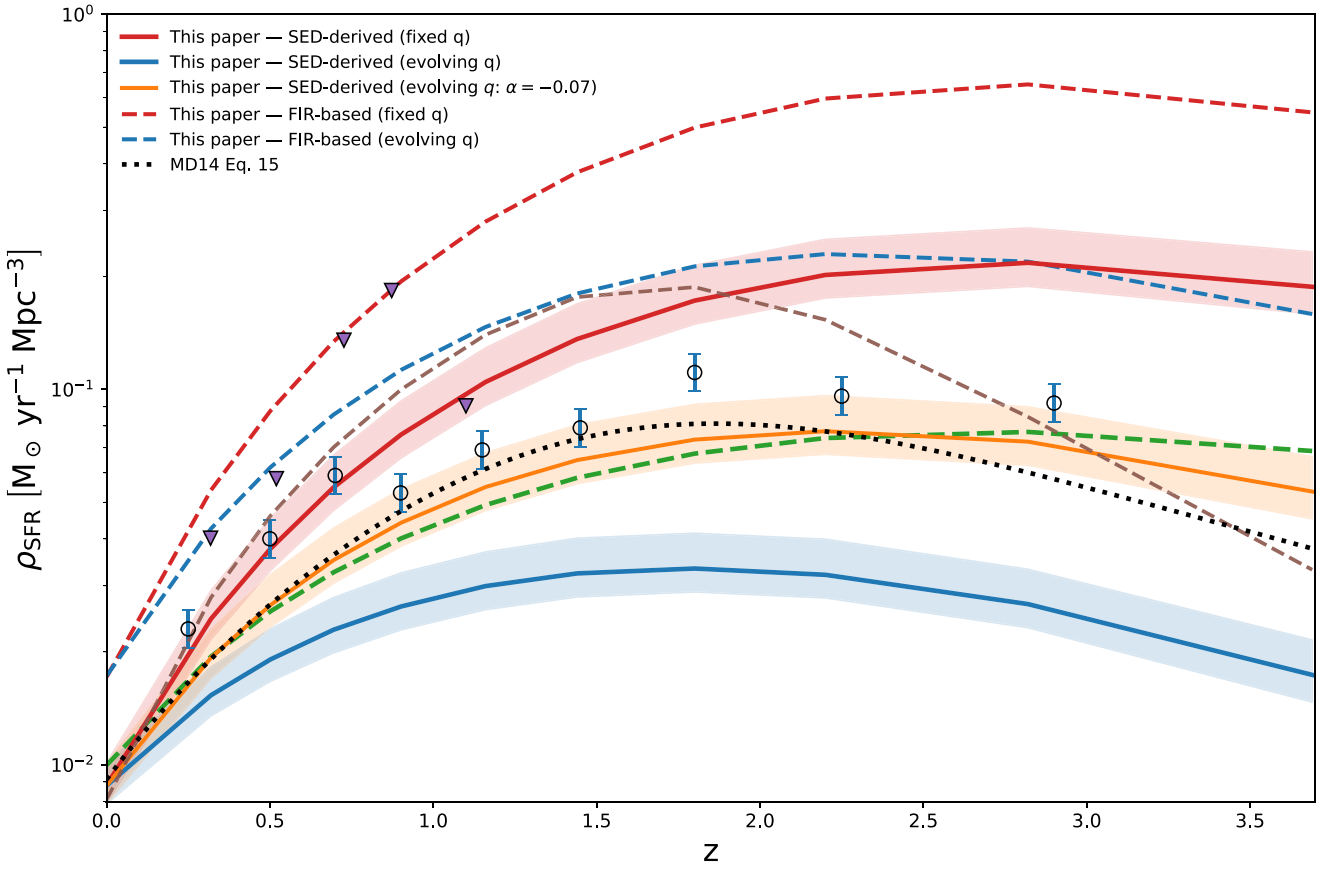

Figure B6. SFRD, $\rho_{\rm SFR}$, as a function of redshift from the single-redshift analysis. Solid lines show the evolution assuming the SED-derived conversion to SFR from radio luminosity (R. H. W. Cook et al. 2024). The fixed-q track is denoted by the red curve (with 68 per cent confidence band) and the evolving-q track by the blue line (with 68 per cent confidence band). We also show an alternative line with $q_{\rm tot} \propto (1+z)^{-0.07}$ (orange). For comparison, the dashed lines show the SFRD based on the FIR-based conversion from radio luminosity to SFR with fixed-q (red) and evolving-q (blue). The brown dashed curve shows the radio-only model from A. M. Matthews et al. (2021). We also show data points from radio-derived SFRD measurements from various literature: M. Novak et al. (2017) (green dashed line), R. K. Cochrane et al. (2023) (open circles with blue error bars) and A. M. Matthews et al. (2024) (purple inverted triangles). The black dotted line is the UV + IR compilation fit of P. Madau & M. Dickinson (2014). We only show the confidence region for our baseline model for clarity.

APPENDIX C: RLFS AND EVOLUTION PARAMETERS FOR COSMOS AND XMM–LSS

This appendix presents RLFs derived separately for the COSMOS and XMM–LSS fields, together with their corresponding evolution parameters. These field-by-field measurements allow us to assess the consistency of the RLF shapes, evolution trends, and fitted parameters across the two MIGHTEE fields. The resulting luminosity functions are shown in Figs C1 and C2.

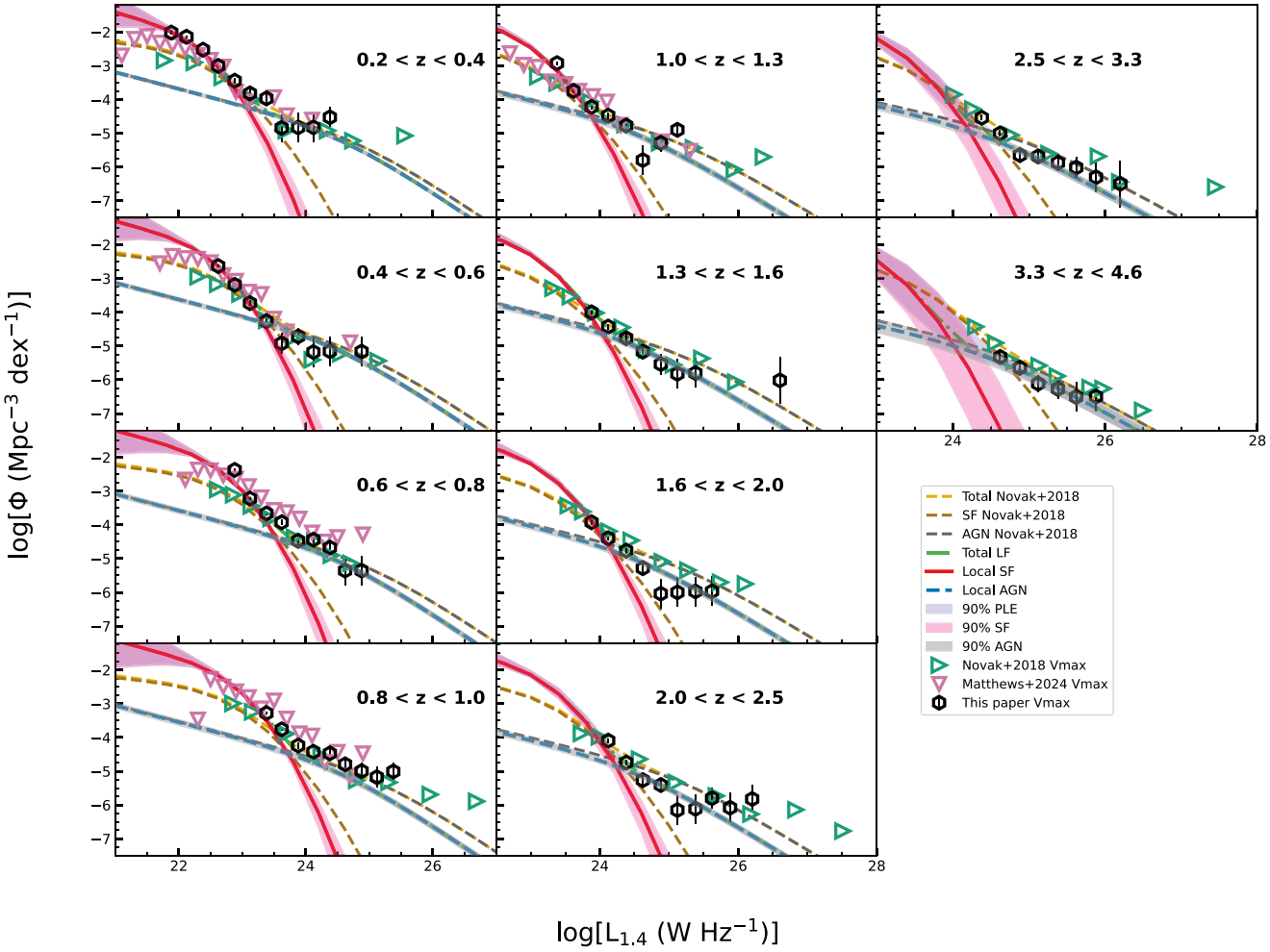

Figure C1. Total 1.4 GHz radio luminosity function in ten redshift bins for the COSMOS field. Black hexagons: $1/V_{\rm max}$ measurements from this work, including statistical redshifts for radio sources without optical/NIR counterparts at $z > 1$. Red solid and blue dashed curves: best-fitting SF (PLE) and AGN (PDE) components for COSMOS; magenta and light-blue bands show their 90 per cent credible intervals.

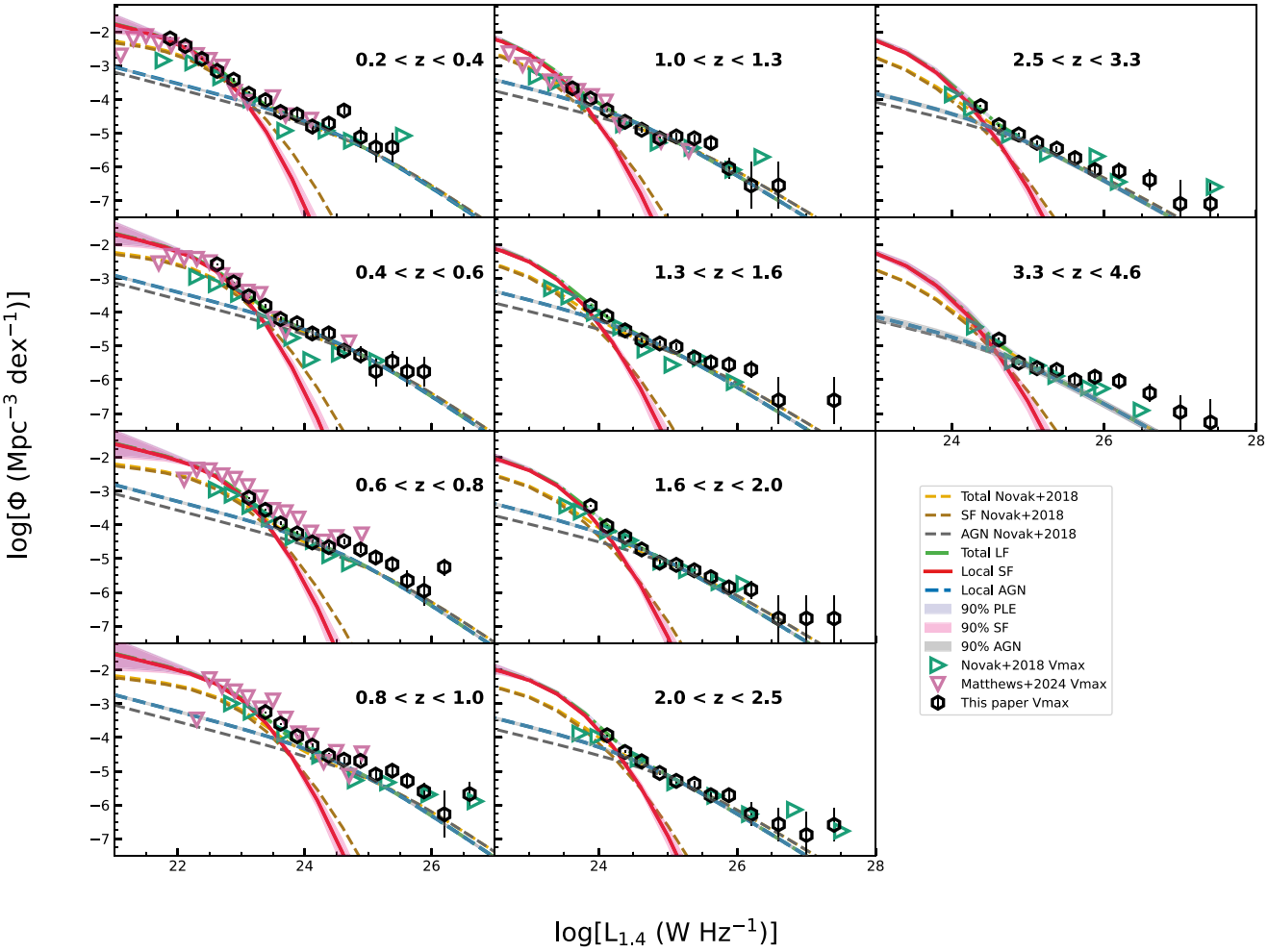

Figure C2. Total 1.4 GHz radio luminosity function in ten redshift bins for the XMM–LSS field. Black hexagons: $1/V_{\rm max}$ measurements from this work, including statistical redshifts for radio sources without optical/NIR counterparts at $z > 1$. Red solid and blue dashed curves: best-fitting SF (PLE) and AGN (PDE) components for XMM–LSS; magenta and light-blue bands show their 90 per cent credible intervals.

This paper has been typeset from a TEX/LATEX file prepared by the author.